Ni-Co-O anodes for the alkaline oxygen evolution reaction: Multistage electrode optimization and plasma-assisted activity enhancement enabled by a coherent workflow

Vineetha Vinayakumar*, Timo Wagner, Christian Marcks, Jacob Johny, Garlef Wartner, Marc F. Tesch, Ioannis Spanos, Aliakbar Ghafari, Adarsh Jain, Oleg Prymak, Ignacio Sanjuán, Ahammed Suhail Odungat, Osama Anwar, Mohit Chatwani, Aneeta Jose, Vimanshu Chanda, Axel Knop-Gericke, Corina Andronescu, Anna K Mechler, Nicolas Wöhrl, and Doris Segets*

V. Vinayakumar, A. Jain, A.S. Odungat, O. Anwar, M. Chatwani, A. Jose, D. Segets
Institute for Energy and Materials Processes – Particle Science and Technology (EMPI-PST)
University of Duisburg-Essen
Carl-Benz-Straße 199, 47057 Duisburg (Germany)
E-mail: vineetha.vinayakumar@uni-due.de; doris.segets@uni-due.de

T. Wagener, N. Wöhrl
Faculty of Physics, University of Duisburg–Essen (UDE), Duisburg (Germany)

C. Marcks, A. K. Mechler
Electrochemical Reaction Engineering
RWTH Aachen University
Forckenbeckstraße 51, 52074 Aachen (Germany)

J. Johny, G. Wartner, M.F. Tesch, I. Spanos, A. Ghafari, A. Jose, A. K. Gericke
Max Planck Institute for Chemical Energy Conversion
Stiftstr. 34-36, 45470 Mülheim an der Ruhr (Germany)

G. Wartner, A. Ghafari, A. K. Gericke
Fritz-Haber-Institute of the Max-Planck-Society,
Department of Inorganic Chemistry,
Faradayweg 4-6, 14195 Berlin (Germany)

O. Prymak
Institute for Inorganic Chemistry and Center for NanoIntegration (CENIDE), University of Duisburg-Essen, Universitätsstr. 5–7, 45117 Essen (Germany)

I. Sanjuán, V. Chanda, C. Andronescu
Chemical Technology III, University of Duisburg-Essen, Carl-Benz-Str. 199, 47057 Duisburg (Germany)

V. Vinayakumar, D. Segets, N. Wöhrl, I. Sanjuán, C. Andronescu
Center for Nanointegration Duisburg-Essen (CENIDE)
University of Duisburg-Essen
Carl-Benz-Straße 199, 47057 Duisburg (Germany)

Keywords: alkaline water electrolysis, plasma processing, ultrasonic spray coating, operando analysis, ink formulation, in-line processing

Abstract

Ni-Co-based oxides (Ni-Co-O) are promising oxygen evolution reaction (OER) catalysts due to their adaptable structures, affordability, abundance, and strong electrochemical performance. While various studies explored the structure-activity relationships and OER mechanisms in these catalysts, comprehensive anode development requires a systematic workflow covering all stages of catalyst optimization. Here, we present an integrated approach for characterizing commercial Ni-Co-O nanomaterials using a combination of analytics during processing, in operando, and post-catalysis to gain insights into parameters influencing anode performance. Key findings include the critical impact of catalyst ink optimization through solvent matrix screening, enabling high-quality electrode layers via ultrasonic spray coating on Ni plates. These Ni-Co-O layers, tested as anodes in alkaline OER, were further enhanced by plasma post-processing, resulting in binder-free surfaces with increased porosity and wettability compared to untreated samples. Notably, plasma treatment also promoted a more redox reversible catalyst structure, improved Fe uptake efficiency, and led to a significantly enhanced OER activity by reducing the overpotential by ~43 mV at 100 mA/cm² compared to untreated samples. Our study highlights the importance of a holistic evaluation approach, from catalyst powder to post-

mortem analysis, that enabled us to discover how plasma post-processing can yield binder-free electrodes with superior electrochemical properties.

1. Introduction

The urgent need to develop renewable and clean energy solutions, driven by the depletion of fossil fuels and the imperative to combat global warming, has propelled hydrogen as a promising alternative for energy storage characterized by zero pollution, high specific energy density, and abundant sources. [1-3] Electrochemical water splitting, evolving over two centuries since its discovery in the 18th century, is becoming pivotal for large-scale hydrogen production. [4] Despite its potential, challenges like production cost and efficiency directly influence its advancement. [5] Even though significant progress in industrial alkaline and acidic water electrolysis has been achieved, the oxygen evolution reaction (OER) at the anode remains a critical bottleneck due to the sluggish kinetics. [6, 7] Catalysts play a vital role in enhancing OER efficiency by reducing overpotential and improving electrocatalytic performance. [8, 9] Current research efforts are thus concentrated on developing highly active OER electrocatalysts to advance further in the overall efficiency and materials-stability during electrocatalytic water splitting. [10, 11] The ideal OER electrocatalyst should possess high intrinsic activity and demonstrate long-term electrochemical stability to withstand harsh reaction environments. [12]

The current benchmark OER electrocatalysts are based on precious metals (e.g., Ir and Ru) and their oxides (e.g., IrO_2 and RuO_2). [13-16] However, their low abundance, high cost, and poor chemical stability in alkaline media pose a challenge to their tenable application and hence demand the use of catalysts based on more earth-abundant and economic elements. [17-19] Hence, significant efforts have been directed toward developing efficient OER catalysts using non-precious transition metals. [20, 21] Examples include materials based on nickel (Ni), cobalt (Co), iron (Fe), and manganese (Mn) which have garnered substantial interest from researchers due to their tunable physicochemical properties and electronic structures that could be used to tune the resulting electrochemical activity. [22-26] In particular, combinations of different metals from this library such as Ni and Co are favored for their adjustable chemical reactivity, theoretical efficiency, and stability under alkaline conditions. [27-29] Ni-Co-based electrocatalysts also possess suitable atomic and electronic structures exposing more active sites and atomic defects, which show high activity, stability, and corrosion resistance during the OER process. [25, 30]

Next to the intrinsic properties of the catalyst, the characteristics of the final anode (the electrode at which OER occurs) are equally important for defining the electrochemical activity and stability in a setting relevant to technical application. This includes features such as the

morphology and particle size, adhesion properties, wetting, and surface roughness of the final electrode, which can all impact its final performance. To date, several physical, chemical, and colloidal deposition techniques have been used to obtain anodes. [31] One promising method among these is ultrasonic spray coating, which involves the spray deposition of an ink containing the desired material onto a suitable support, thus achieving a compact active layer. In the case of the electrode fabrication by ultrasonic spray coating, the process involves multiple stages starting from the powder material preparation followed by the formulation of a stable catalyst ink and final spray deposition to obtain solid electrodes. This demands characterization and continuous optimization throughout the entire process chain rather than focusing on only one stage during the anode development. Optimization of the electrode in each stage is crucial as this affects the following stage and defines the extrinsic properties of the final anodes and their performance. [32] However, comprehensive studies encompassing full system characterization and optimization within a coherent workflow remain rare, particularly for critically important material systems such as Ni-Co-based anodes for alkaline water electrolysis.

Herein, we present a coherent workflow for Nickel-Cobalt-oxide (Ni-Co-O) for alkaline OER through the entire anode development chain. Our investigations start with a thorough characterization of the commercial Ni-Co-O powder, followed by the development and formulation of a stable catalyst ink, and final fabrication of electrodes on Ni plates through ultrasonic spray coating. In each step, we utilized a set of tools to identify and optimize crucial properties that influence the final application of these electrodes. At the end of the electrode deposition stage, surface morphology changes along with the removal of the binder are induced by anode layer post-processing under N_2-plasma, significantly enhancing the OER performance. Our in-depth pre- and post-electrocatalyst analysis by X-ray absorption spectroscopy together with *operando* Raman studies between the as-prepared and plasma-treated films correlate the higher plasma-induced activity to both, an enhanced Fe-uptake efficiency, and improved structural redox flexibility of plasma-treated anodes compared to their as-prepared counterparts. By closing the loop from powder studies to layer property assessment before and after plasma-post-processing, electrochemical characterization, *operando,* and post-mortem studies, the developed coherent workflow enables a continuous and knowledge-based electrode advancement within the available wide parameter space.

2. Results and discussion

2.1. Characterization of the Ni-Co-O powder

2.1.1. Particle size and composition analysis

The Ni-Co-O commercial powder was first thoroughly characterized by a set of complementary analytical techniques before being used in the subsequent steps, i.e., generating Ni-Co-O catalyst inks, followed by their coating on Ni plate substrates. Initially, transmission electron microscopy with energy dispersive X-Ray spectroscopy (TEM-EDX) was employed to evaluate the morphology of the Ni-Co-O particles as well as their bulk composition. **Figure 1** depicts a typical TEM image together with the crystal structure and EDX maps of the Ni-Co-O particles. The commercial Ni-Co-O particles exhibit a cube-like shape with largely varying primary particle sizes in the range 10-150 nm (Figure 1a) with a mean particle size (diagonally measured on more than 200 particles) of 54±41 nm (inset). Figure 1b depicts the selected area electron diffraction (SAED) analysis performed on the Ni-Co-O particles that evidenced a polycrystalline structure with crystal reflections along different planes. To verify the crystal structure, the d-spacings along different planes were measured and compared with standard JCPDS data for a face-centered cubic (FCC) structure of substituted Ni-Co-O phase with lattice parameter 4.2156 Å. The corresponding standard JCPDS files for NiO (47-1049, a= 4.1771 Å [33]) and CoO (48-1719, a=4.2612 Å [34]) were used to illustrate the FCC structure of the Ni-Co-O.

Interplanar spacings of 2.4, 2.1, and 1.49 nm were measured which correspond to the (111), (200), and (220) planes of FCC Ni-Co-O. In the case of Ni-Co-O, the estimated d-spacing values show slight shifts from that of the pristine NiO or CoO, thus confirming a solid solution mixture. [35] In agreement with the SAED measurements, the high-resolution TEM (HRTEM) image in Figure 1c clearly shows crystalline Ni-Co-O particles where the average value of the interplanar distance measured was 0.24 nm which corresponds to the (111) reflection from the FCC Ni-Co-O. It is worth noting that the used Ni-Co-O powder does not contain the binary nickel cobaltite ($NiCo_2O_4$) which exhibits a cubic structure with different crystal parameters. [36]

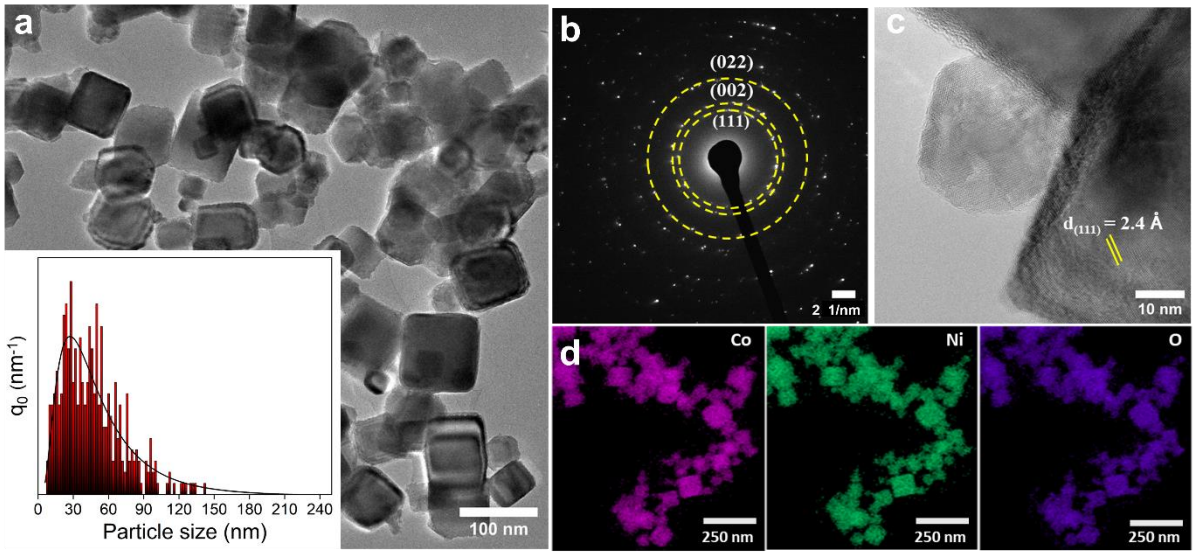

Figure 1 *(a) TEM image of Ni-Co-O powder showing cubic-shaped particles with the size histogram in the inset; (b) SAED pattern showing the polycrystalline structure with selected crystal reflections marked; (c) HR-TEM image of a crystalline Ni-Co-O particle with the measured interplanar spacing marked; (d) EDX map showing a homogeneous distribution of Co, Ni, and O in each particle. Scale bars are given in the respective images.*

The energy dispersive X-ray analysis (EDX) on the Ni-Co-O particles confirmed the presence of all expected elements (Ni, Co, and O) in each particle as shown in Figure 1d. This excludes the presence of individual, coexisting NiO and CoO phases in these particles, in line with the specifications of the manufacturer. The average bulk composition showed almost equal Ni and Co concentrations (20 and 19.2 at% for Co and Ni, respectively) (**Figure S1**).

2.1.2. Structure and surface chemical analysis of the powder

After characterizing individual Ni-Co-O particles by TEM, we conducted X-ray diffraction (XRD), Raman spectroscopy, and X-ray photoelectron spectroscopy (XPS) on the powder ensemble to further confirm the crystal structure, phases, and surface composition. By XRD analysis on the Ni-Co-O powder (**Figure 2a**), we identified five major reflections at 2θ values of 36.9, 42.9, 62.2, 74.6, and 78.5° corresponding to the (111), (200), (220), (311), and (222) crystal planes of a single FCC structure. It has to be noted that all these identified reflections show a slight shift in their positions from the standard NiO (ICDD # 65-2901) or CoO (ICDD # 74-2391) phases and thus underline the formation of a different FCC solid solution with a lattice parameter value of 4.22 Å within the space group *Fm-3m* as determined from Rietveld

refinement. According to Vegard's law which defines a linear relationship between the molar ratios of the constituent elements and the lattice parameter of the resulted alloy, [37] both phases CoO and NiO are present in an approximately equal ratio of 50:50. These XRD results agree well with a previously reported study on a NiO-CoO solid solution obtained by calcination of a $Ni(NO_3)_2$ and $Co(NO_3)_2$ mixture. [38] Overall, the XRD results further confirm the single FCC phase in the Ni-Co-O powder excluding segregation into individual NiO or CoO phases, and thus agree well with the previous SAED and HRTEM results.

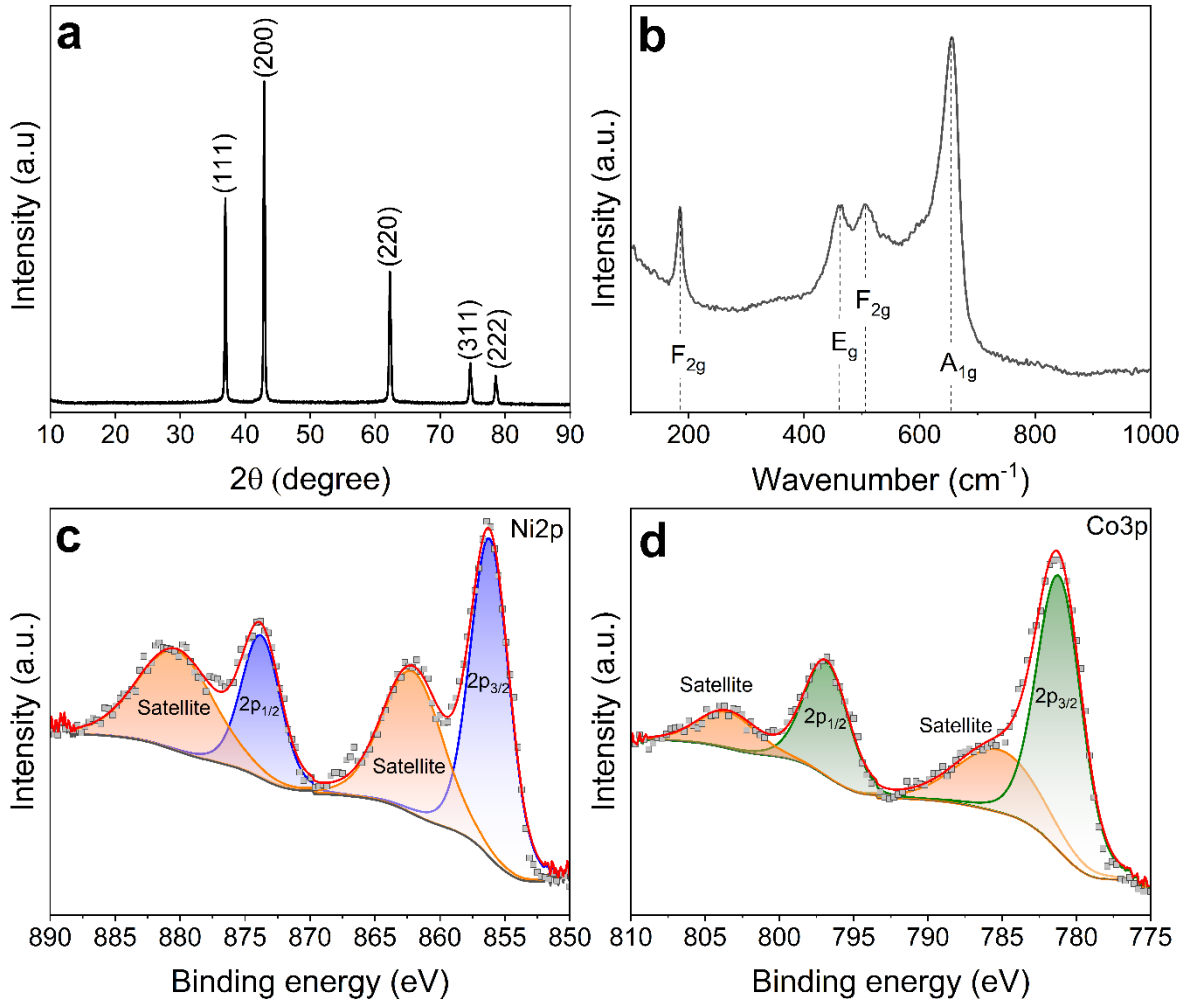

Figure 2 *(a) XRD pattern; (b) Raman spectrum; (c) Ni2p high-resolution and (d) Co2p high-resolution XPS peaks of the Ni-Co-O powder sample.*

The Raman spectrum of the Ni-Co-O powder is characterized by four major Raman bands located at 185, 462, 506, and 656 cm^{-1} as shown in Figure 2b. These bands correspond to the F_{2g}, E_{2g}, F_{2g}, and A_{1g} vibrational modes of Co-O and Ni-O vibrations and are close to those reported for $NiCoO_2$ thus validating a single-phase Ni-Co-O in the powder. [39]

The surface composition of the Ni-Co-O powder was further analyzed by XPS. Figures 2c and d show XPS high-resolution spectra of Ni2p, and Co2p regions, respectively. The Ni2p spectrum is deconvoluted and separated into four components, the two spin-orbit-split Ni $2p_{3/2}$ and $2p_{1/2}$ excitations together with two associated satellite peaks (Figure 2c). The $Ni2p_{3/2}$ and $Ni2p_{1/2}$ peaks are located at binding energy values of ~856.2 and ~873.8 eV aligning with Ni bound to oxygen, thus excluding the presence of metallic Ni in the powder. [40] The Co 2p spectrum, constituted by the spin-orbit-split 2p peaks and 2 satellite peaks, show binding energy positions of ~781.2 and 796.8 eVs for the Co $2p_{3/2}$ and $2p_{1/2}$) peaks (Figure 2d) as well as the satellite peaks located at ~785.2 and ~803.5 eV. Together with the previous discussions, this confirms the presence of a Ni-Co-O phase. [41] Although the existence of Ni and Co as oxides can be confirmed, a detailed analysis of the exact oxide phases and quantification of Ni to Co ratio only from the 2p regions in XPS is challenging because of an overlap of Auger features of nickel (hydr)oxide in the Co2p region, and cobalt (hydr)oxide in the Ni2p region. [42] To estimate the Ni/Co ratio on the surface, the 3p region of Ni and Co was thus analyzed, resulting in 51 % Ni and 49 % Co in the powder samples. This is in line with the nominal composition of the Ni-Co-O powder and close to the composition that was previously estimated from XRD (NiO:CoO ~ 50:50). This also indicates that the Ni-Co-O powder used here shows an almost equal bulk and surface chemical composition.

2.1.3. Dispersibility by Hansen solubility parameters (HSP)

Understanding the intricate relationship between probe liquids and catalyst materials in a colloidal dispersion is crucial since liquids are used to transport catalyst materials throughout the coating and drying process. Hence, after thoroughly characterizing the Ni-Co-O powder in the dry state, we analyzed the powder-liquid interaction with probe liquids of known polarity to assess the particles' surface properties and to rationally select the composition of the continuous phase for the ink formulation.

According to HSP, the three parameters from dispersion forces (δD), dipolar intermolecular force (δP), and hydrogen bonds (δH) between probe liquids and catalyst particles can be represented as coordinates in the three-dimensional Hansen space. [43, 44] In line with our previous works, we used the two-step procedure of Amin et al. to select the appropriate probe liquids. [45] In the first step, all three initial probe liquids namely ethanol (EtOH), dimethylformamide (DMF), and tetrahydrofuran (THF), formed good dispersions with Ni-Co-O. This meant that the material interacted well with all protic, aprotic, and polar probe liquids. Hence, in the second

step, isopropanol (IPA), acetone (Ace), dimethyl sulfoxide (DMSO), 1,4. Dioxane (Diox) and toluene (Tol) were added.

The relative sedimentation times, determined from integral extinctions of the sedimenting dispersions, were used to rank these eight probe liquids from the best to the least compatible solvent (details in section 4.2.1). The HSPiP program was used to calculate the HSP of the material using the automated-addition-method developed by Süß et al. [46] Accordingly, the resulting HSP of Ni-Co-O and sphere are shown in **Figure 3**.

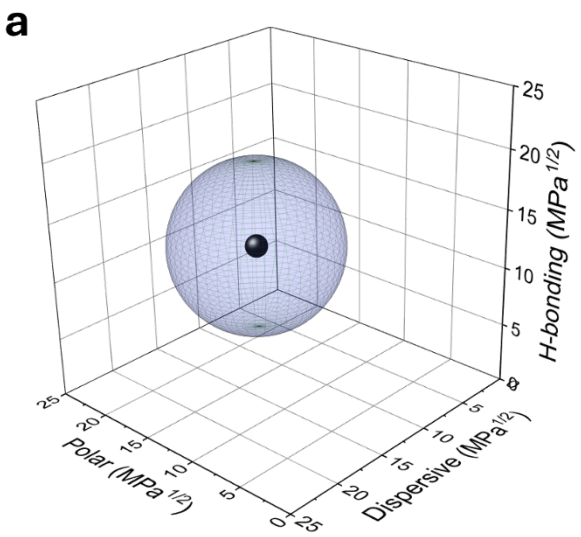

Material	Ni-Co-O
Disperse interactions δ_D ($MPa^{1/2}$)	15.2
Polar interactions δ_P ($MPa^{1/2}$)	12.3
Hydrogen bonding δ_H ($MPa^{1/2}$)	13.6
Sphere radius ($MPa^{1/2}$)	6.9
Outliers	0
Fitting	1

Figure 3 *HSP determination of Ni-Co-O with probe liquid selection done by the two-step procedure followed by automated addition to determine the final HSP. The HSP of Ni- Co-O (a) is shown with the sphere outline representing the region of good interaction with solvents, while HSP coordinates are summarized in the table on the right.*

This study reveals a higher contribution to hydrogen bonding interactions and dipolar interactions allowing the catalyst powder to disperse readily in most of the probe liquids. Here, it should be noted that water was not considered within the given HSP sphere due to its high hydrogen bonding capabilities (δH = 42 $MPa^{1/2}$), making a large distance compared to other chosen solvents. [45] However, due to cost considerations and since water is one of the commonly used liquids in generating stable catalyst inks, we included water in the final ink formulations. [47]

2.1.4. Ni-Co-O ink formulation

The sedimentation behavior of catalyst nanopowders in different solvent systems is shown in **Figure 4**. Transmittograms [48] were used to analyze dispersions prepared in both pure water and a water-ethanol mixture with Nafion binder. These transmittograms, which are contour plots illustrating time- and space-resolved transmission data, were generated from centrifugation data to offer insights into sedimentation dynamics and colloidal stability.

In each transmittogram, the x-axis represents the elapsed time since centrifugation began, and the y-axis shows the radial position within the centrifuge cell. Transmission values are represented by varying gray tones, with darker tones indicating higher levels of light blockage due to scattering, corresponding to higher particle concentration at a given time and position.

Figure 4 compares sedimentation profiles for the two solvent systems: (a) pure water and (b) a 1:1 water-ethanol mixture, both containing Nafion as the binder. In the pure water system (Figure 4a), sedimentation occurs quickly, with high transmission levels appearing early in the process and minimal gradient development, suggesting rapid particle settling. In contrast, the water-ethanol mixture (Figure 4b) exhibits slower sedimentation with a more gradual transmission gradient over time, indicating a reduced particle settling rate and improved stability.

Under a relative centrifugal acceleration (RCA) of 733.69, complete sedimentation of particles in the water-based dispersion occurred in approximately 8 minutes, equivalent to roughly 4 days, and 8 hours under stationary conditions (RCA = 1). For the water-ethanol mixture, complete sedimentation took approximately 25 minutes, translating to around 13 days and 2 hours under stationary conditions. The slower sedimentation rate observed with the water-ethanol system suggests that this solvent combination improves colloidal stability, potentially making it more suitable for applications requiring prolonged stability and homogeneous anode layers. [49]

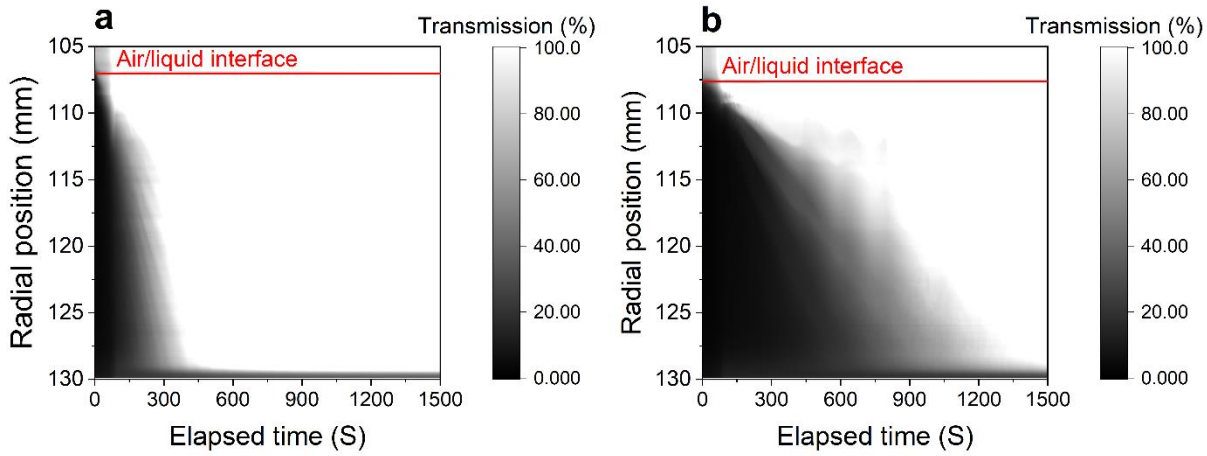

Figure 4 *Visualization of the time-resolved sedimentation process via transmittograms: (a) Ink prepared using pure water as a solvent, (b) ink prepared using a mixture of water and ethanol as continuous phase (1:1 volume ratio), both containing Nafion as a binder.*

2.2. Ni-Co-O layer deposition and plasma post-treatment

Coated Ni-Co-O layers were obtained by spray deposition of the Ni-Co-O ink onto Ni plate substrates (**Figure 5a**), for details see section 4.3. Ultrasonic spray coating possesses several advantages in general such as good reproducibility and transfer efficiency, precise conformal coating, and simplicity. [50] After the deposition of the layers on Ni plates, the resulting Ni/Ni-Co-O samples were post-treated under a nitrogen plasma. Plasma treatment was applied due to its capability to induce changes in the surface properties, such as morphology, wettability, as well as chemical composition, in particular altering the oxide phases which are all crucial in alkaline water electrolysis. [51, 52] A first indication for a successful modification of the surface is given already by a change in visual appearance, as the plasma-processed electrodes appeared darker compared to the as-prepared Ni-Co-O layers (**Figure S2**). A comprehensive analysis of the plasma-induced changes in the physicochemical properties of the anode is discussed in detail in the following sections.

2.2.1 Surface topography of the Ni-Co-O layers

To identify the surface of the electrodes before and after plasma treatment, scanning electron microscopy (SEM) analysis was performed on the coated Ni-Co-O layers. When Kong et al. applied post-treatment by nitrogen plasma onto NiCo-layered double hydroxide (LDH), the surface was distorted and roughened, and they found a higher density of micropores and mesopores which were attributed to the bombardment of the energetic particles and active

hydrogen-mediated etching inside the plasma. [53] Figure 5b and 5c show the surface morphology of the as-prepared and plasma-treated Ni-Co-O at two different magnifications along with the corresponding EDX mappings. Also in our case, a significant transformation of the surface of the coated layers is noted after the plasma treatment. The more spherical particle-like structures in the as-prepared films turn into a more interconnected flake-like structure with apparent higher porosity after the plasma treatment. In particular, it is often reported that a more porous structure of the catalyst layers is advantageous for electrochemical applications because the electrodes exhibit increased surface area and fast mass diffusion leading to enhanced activity. [54] Since the porosity might play a crucial role in their application as electrodes, a more detailed analysis of the pore structure in these spray-deposited Ni-Co-O layers was indispensable.

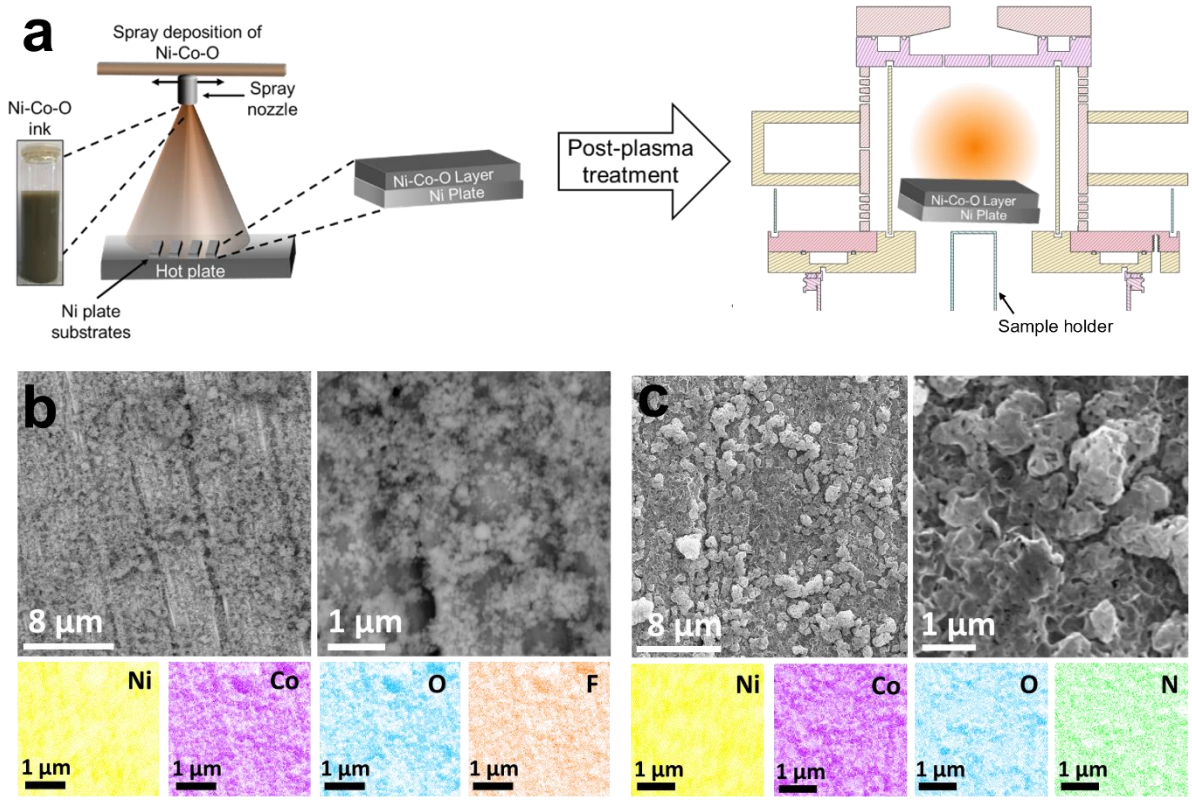

Figure 5 *(a) Schematic representation showing the spray deposition of Ni-Co-O layers on Ni plate substrates and the N_2 plasma post-treatment on the coated layers. SEM and EDX analysis was conducted on the (b) as-prepared and (c) plasma-treated Ni-Co-O films deposited on Ni plate substrates.*

TEM analysis was subsequently conducted to determine the overall appearance of the Ni-Co-O particles on the as-prepared and plasma-treated Ni-Co-O films and to investigate any changes in the particle size after film deposition and plasma post-treatment (**Figure S3**). To this end,

particles were scratched from the spray-deposited layers on the Ni plate and subsequently analyzed. The as-deposited Ni-Co-O layers showed an average particle size of 57 nm (Figure S2a) thus matching the average size obtained for the commercial Ni-Co-O powder (54 nm). Interestingly, plasma post-treatment led to a size reduction of the primary Ni-Co-O particles down to ~14 nm which are more irregularly shaped as shown in Figure S2b. The EDX maps conducted on the as-prepared Ni-Co-O samples identified all expected elements (Ni, Co, and O), and in addition C from the Nafion binder used for the catalyst ink preparation (see experimental section for details). In the case of the N_2 plasma-treated Ni-Co-O particles, in addition to the homogeneous distribution of Ni, Co, and O in the layer, N was also detected.

To evaluate the topography of the anodes in more detail, atomic force microscopy (AFM) was employed and analyzed by multi-stage data quantification (MSDQ). [47] Parameters utilized in primary AFM studies are given in **Table ST1**. **Figure 6a, b** shows the surface topography of the as-prepared and plasma-treated Ni-Co-O samples. The as-prepared sample has a higher maximum surface height of 3.7 μm, which reduces to 2.5 μm after plasma treatment. This visualization indicates that plasma treatment has impacted the surface height variation, aligning with the previously discussed SEM top-view analysis. To further substantiate this observation, we analyzed two surface features: surface roughness (representing height variation) and homogeneity score (indicating the distribution of particles over the measured area of 100 × 100 μm^2). These features are visualized using a 2D kernel plot in Figure 6c. [49] As expected, the reduction in surface roughness after plasma treatment correlates with an increased homogeneity score and it is clearly seen that the exposure to the N_2 plasma significantly alters the morphology and thus microstructure of the anodes.

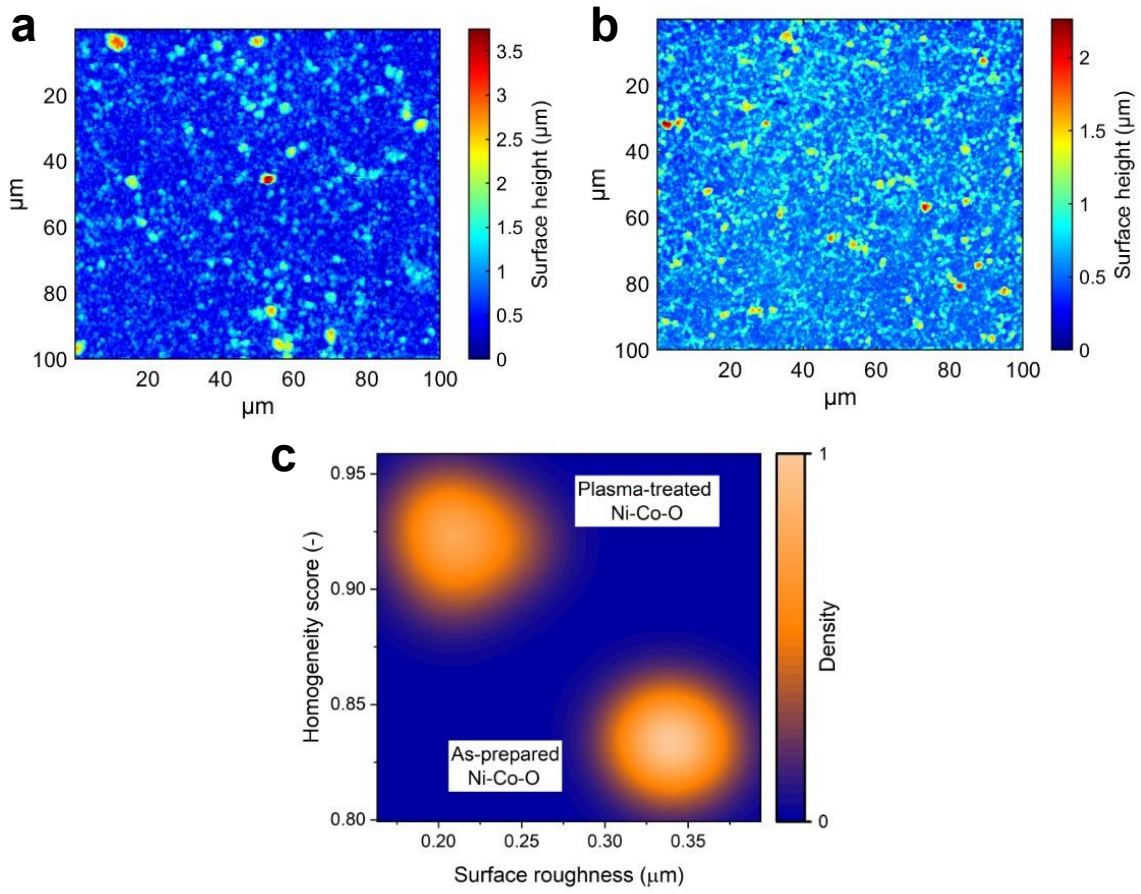

Figure 6 *AFM-MSDQ analysis: Topographical images of (a) as-prepared Ni-Co-O layer and (b) plasma-treated layer. (c) 2D distribution of surface roughness and homogeneity score of as-prepared and plasma-treated anodes.*

2.2.2 Cross-section and pore network of the Ni-Co-O layers

To evaluate the differences in pore sizes between the as-prepared and plasma-treated samples, focused ion beam (FIB)-SEM was employed. **Figure 7** shows cross-section images of the as-prepared, and the plasma-treated Ni-Co-O anodes, respectively. The pore coverage is defined as the portion of void space within the catalyst layer and is a crucial parameter that affects mass transport and access to active sites, directly influencing the catalytic performance of the layer. [55] The estimated pore coverage in the as-prepared and plasma-treated Ni-Co-O layers (both with thicknesses in the range 350-400 nm) are 11 and 14 %, respectively, along with a slight expansion of the coated layer after the plasma treatment. While a clear boundary with less pore density is observed at the interface between the substrate and the catalyst layer in the as-prepared films (highlighted by the horizontal dashed line in 7a), the plasma-treated films show a much smoother interface. We assume that the interaction of the deposited Ni-Co-O layers

with the charged species in the plasma might have led to enhancing the contact between the coated layer and the substrate, likely induced by a layer rearrangement due to the energy input and the removal of the binder. This results in a more uniform layer and a smoother substrate-coated layer interface after the plasma treatment. The higher pore density in the plasma-treated Ni-Co-O films is also further validated by mercury intrusion porosimetry (MIP) measurements (**Figure S4**) where in particular the abundance of pores of sizes starting from 200 nm is much higher in the plasma-treated layers. It is worth noting here that porous structures are expected to be beneficial for electrocatalytic water splitting as they can provide more surface active sites and enable easier mass diffusion. [54]

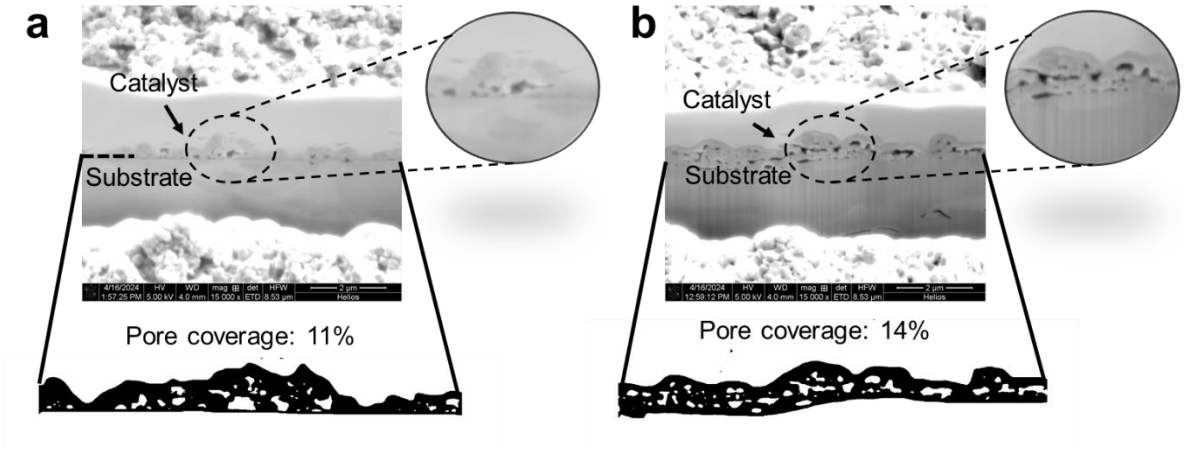

Figure 7 *FIB-SEM images showing the pore coverage in both (a) as-prepared and (b) plasma-treated Ni-Co-O layers. The horizontal dotted line in (a) indicates the boundary between the coated Ni-Co-O layer and the substrate and zoom-in images are given for better clarity.*

2.2.3 Crystal structure, surface composition, and wettability of Ni-Co-O layers

After understanding the microstructure of the as-prepared and plasma-treated Ni-Co-O samples in detail, we now turn to the crystal structure and surface chemical state analysis of these layers. XRD was performed on the coated layers before and after the plasma treatment to identify changes in the structure compared to the Ni-Co-O powder precursor and due to the plasma treatment. **Figure 8a** shows the XRD spectra of the as-prepared and plasma-treated Ni-Co-O layers on Ni plates. In general, the deposited Ni-Co-O layer exhibits the same crystal structure as the Ni-Co-O powder (Figure 2a), in addition, the reflections are observed at 2Θ values of 44.5, 51.8, and 76.4° that can be assigned to the Ni substrate with FCC structure ICDD# 04-0850. However, no apparent shift in the Ni-Co-O reflections on the layers was observed either in the as-prepared or plasma-treated layers, confirming that the initial bulk crystal structure of

the powder is preserved in the spray-deposited films and after the post-plasma processing. While lattice parameters of the as-prepared and plasma-treated samples exhibit similar values, the crystallite size decreased after the plasma treatment from ~80 to 74 nm (Figure 8b).

Since XRD is dominated by bulk information, we additionally performed XPS analysis on the as-prepared and plasma-treated Ni-Co-O layers to further explore plasma-induced surface chemical changes, which is highly relevant with respect to the application of the samples as electrocatalysts. [56] Figure 8c depicts XPS survey spectra of both as-prepared and plasma-treated Ni-Co-O layers. The most obvious observation is that the high-intensity F1s peak observed at ca. 690 eV in the as-prepared sample, attributed to the Fluorine in the Nafion binder (see the experimental section 4.2.2 for details), is not present anymore in the plasma-treated sample. Simultaneously, the major C1s contribution in the as-prepared Ni-Co-O is assigned to -CF_2-CF_2- from Nafion which disappears after the plasma treatment along with the emergence of N-containing species (**Figure S5**). Both changes indicate the surface removal of Nafion due to the plasma processing of the layer together with the incorporation of nitrogen. Due to the Fluorine-KLL auger interference (at ~835 eV) in the region of the Ni2p, features analysis of Ni and Co was restricted to the 3p region (Figure 8d). The O, Ni, and Co signals showed a significantly increased intensity after the plasma processing due to Nafion removal from the surface of the Ni-Co-O layer, further corroborating the finding of Nafion removal and the higher availability of Co and Ni sites on the surface upon plasma treatment. Though no obvious changes in the Ni3p and Co3p peak shape could be identified (**Figure S6**), the XPS quantification of the surface composition showed a significant increase in the Ni:Co ratio after the plasma treatment. More than twice Ni (than Co) was found on the plasma-treated Ni-Co-O electrode surface (Figure 8d) due to additional contributions from the Ni substrate.

To compare the surface wettability of the as-prepared and plasma-treated Ni-Co-O layers, contact angle measurements were undertaken. The as-prepared Ni-Co-O electrode is characterized by a hydrophobic surface with a contact angle of ~118^o (**Figure S7**). In contrast, the contact angle of the films after the plasma treatment could not be detected after the layers had undergone the post-N_2-plasma treatment. This is due to the highly hydrophilic surface attributed mostly to the changes that occurred in the surface morphology together with the removal of the binder.

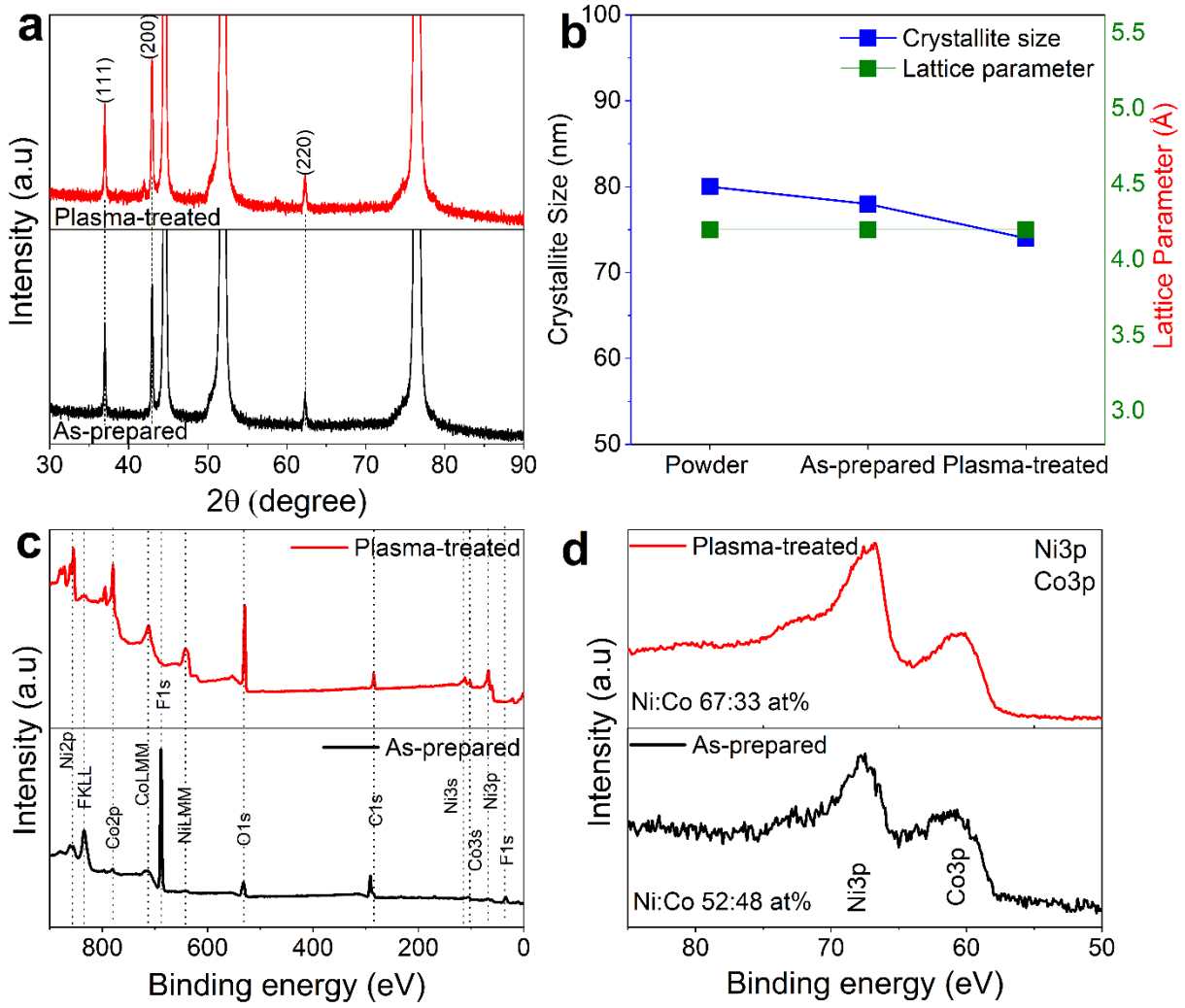

Figure 8 *(a) XRD spectra of the as-prepared and plasma-treated Ni-Co-O films with marked reflections corresponding to the Ni-Co-O FCC phase. The reflections marked by the arrow correspond to the Ni substrate; (b) crystallite size and lattice parameter values derived from Rietveld refinement for both films; (c) XPS survey spectra with significant elemental peaks marked and (d) high-resolution XPS showing Ni and Co 3p region of the films.*

2.3. Electrochemical OER performance of Ni-Co-O anodes

After characterizing the morphology, and physicochemical properties of the Ni-Co-O layers, their electrochemical performance as anodes for the OER was evaluated. **Figure 9a, b** compares the constant operation at 100 mA cm^{-2} for 2 h for as-prepared and plasma-treated Ni-Co-O anodes in a beaker cell configuration, using 1 M KOH electrolyte with controlled Fe concentrations of 15 ppb and 110 ppb.

In the initial study with 15 ppb Fe in KOH (Figure 9a), the coated electrodes demonstrated significantly higher activity, i.e. 113 ± 6 mV lower overpotential at the end of the chronopotentiometry (CP), compared to pristine Ni plate supports. This is logical, as pure Ni electrodes are mostly inactive in low Fe-electrolytes, [57] while the addition of Co enhances the activity of Ni-based electrodes. [58] Furthermore, plasma-treated electrodes showed a notable improvement in the overall reproducibility of the measurement, with an 82 % reduction in standard deviation compared to the as-prepared electrodes, as indicated in the legend. This indicates that plasma treatment effectively altered the surface chemistry and irregularities, leading to more uniform and compact surface structures, which align with the surface topology discussed in Section 2.2.1. Comparing the end-potential after the two hours of CP measurements in the low iron-containing electrolyte, the plasma-treated Ni-Co-O (1.690 V vs. RHE) showed a ~10 mV reduction compared to as-prepared Ni-Co-O (1.698 V vs. RHE). Though small, this difference is significant, especially given the low standard deviation of the plasma-treated samples.

When tested with 110 ppb Fe in KOH (Figure 9b), which is a more realistic iron concentration for alkaline electrolyzers, the plasma-treated layers exhibited a significantly lower overpotential after 2 h at 100 mA cm^{-2} (1.574 V vs. RHE), compared to the as-prepared Ni-Co-O (1.617 V vs. RHE), as demonstrated in Figure 9b. To further underpin these findings, measurements were also conducted in a flow cell configuration, where comparable trends were observed (Figure S8), highlighting the robustness of the plasma-treated catalyst layers across different electrochemical test setups.

The same trend is corroborated by the activity CVs for all samples (**Figure S9a and b**). To better understand this behavior, the conditioning of the electrodes is depicted in Figure 9c and d. For the low iron-containing electrolyte (Figure 9c), the charge passed during the oxidation and reduction of the electrodes is similar for the plasma-treated and the as-prepared sample. However, there is a significant charge increase for the plasma-treated samples in the higher iron-containing electrolyte (Figure 9d). The transferred charge can be linked to the development of an OER-active hydroxide layer during the phase transition from $Ni(OH)_2$ to NiOOH on the catalyst surface at higher potentials, resulting in the formation of a structure resembling Ni_xOOH/Co_xOOH. [59] Mattinen et al. have shown that this oxide formation is dependent on the investigated material but also on the iron concentration in the electrolyte. [60] Hence, we assume that plasma treatment favors the faster formation of Ni_x/Co_x-(Fe)OOH, compared to the as-prepared samples, which is shown in the larger oxidation and reduction peaks. The higher

porosity of the plasma-treated samples could also facilitate the diffusion of the OH-, resulting in a faster conversion of the hydroxide.

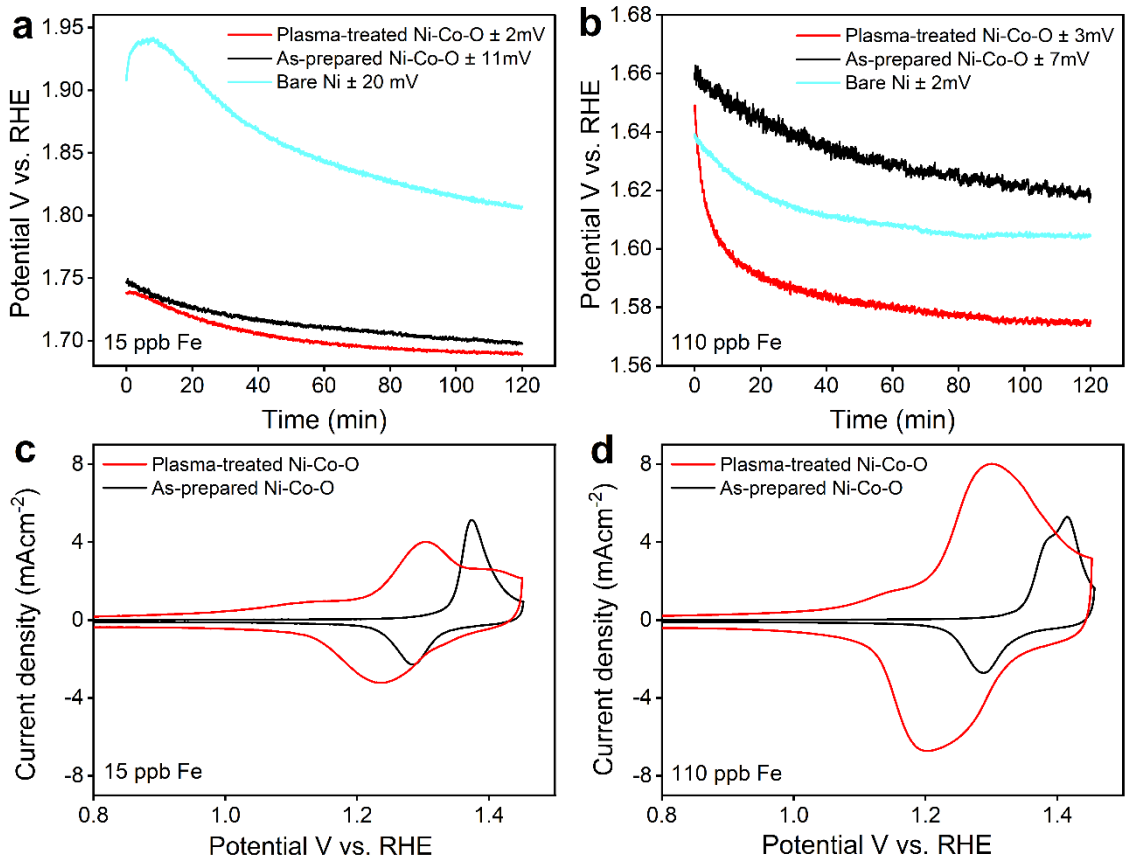

Figure 9 *(a) and (b): Chronopotentiometry (CP) for 2 h at 100 mA cm^{-2}of as-prepared and plasma-treated Ni-Co-O electrodes measured in a beaker cell in 1 MKOH containing (a) 15 ppb and (b) 110 ppb Fe. Electrochemical conditioning of anodes in (c) 15 ppb and (d) 110 ppb containing 1 M KOH. Shown is the last of 50 cycles with a scan rate of 100 mV s^{-1} for a potential window of 0.2 V vs. RHE and 1.45 V vs. RHE.*

Interestingly, in the higher iron-containing electrolyte, the performance of the bare Ni support is better than the as-prepared samples (1.605 V vs. RHE after 2 h CP at 100 mA cm^{-2}, Figure 9b). We assume that for the bare nickel, the active Ni_xFe_x-OOH species forms during the conditioning of the samples, [59] due to the now elevated iron in the electrolyte. In low iron-containing electrolytes, conditioning of nickel will still improve its activity, however, the absolute activity is still significantly worse as compared to higher iron-containing electrolytes. [58] This process could be faster for the bare nickel compared to the Ni-Co-O, due to the already oxidized state of the powder-based anodes, needing more time for the restructuring of the surface into a similar $Ni_x/Co_x/Fe_x$ – OOH species.

It is important to consider that the electrochemical active surface area (ECSA) of as-prepared and plasma-treated samples may differ due to their distinct surface morphologies (Figure 5b, c), making an evaluation of ECSA highly relevant. To investigate this, ECSA measurements were performed for the beaker cell experiments using rapid CV cycling, as described in the literature. [61] However, the capacitance values obtained should be interpreted with caution, as the measured double-layer charging may overlap with effects such as continuous Ni and Co oxidation. Despite this limitation, the capacitance values (**Table ST2**) showed a clear increase for the plasma-treated samples compared to the as-prepared ones. While we refrain from directly correlating this to larger ECSAs, the data qualitatively suggests that plasma treatment induces noticeable morphological changes.

So far, we hypothesize that plasma treatment may favor the formation of hydroxides, improve gas bubble transport due to an altered pore structure, remove Nafion from the surface, and induce defects, thereby exposing more active sites for the reaction. Altogether, this demonstrates the role of the Fe concentration in enhancing the catalytic performance and – freelance of the test setup, underscores the effectiveness of plasma-treated Ni-Co-O anodes for the alkaline OER. To better understand the impact of plasma treatment of Ni-Co-O on the OER performance, we conducted X-ray absorption spectroscopy (XAS) measurements on pre- and post-electrochemical samples, along with *operando* Raman analysis. These results are discussed in the following section.

2.4. XAS and operando Raman measurements on Ni-Co-O anodes

Since the XPS analysis was complex for the Nafion-containing as-prepared Ni-Co-O films, to further evaluate the changes of the near-surface electronic structure induced by the plasma treatment, we applied a multi-element analysis by XAS in total electron yield (TEY) mode at the N, O and F K-edge, as well as at the Fe, Co and Ni L-edges. To obtain knowledge about further surface changes induced during electrochemistry, samples were also analyzed after electrochemical characterization. Comparison of Ni and Co L-edge spectra with different reference spectra demonstrates that before the plasma treatment, Ni and Co were both mainly in a 2+ oxidation state (**Figures S10 and S11**). The main features of the O K-edge spectrum of the plasma-treated sample coincide with the main features of the Ni- and Co-oxide reference spectra (**Figure 10**). The vertical lines in Figure 10 facilitate a direct comparison of the main spectral features with corresponding references. In the spectrum of the as-prepared sample, these features are superimposed by the contributions that we assign to O in the Nafion binder.

These findings are in line with the presence of the mixed oxidic rock salt Ni-Co-O phase in both, the as-prepared and plasma-treated layers. Spectroscopic changes of the Ni and Co L-edges after plasma treatment indicate partial oxidation of Ni^{2+} to Ni^{3+} (indicated by a slight intensity increase at 854.6 eV, Figure S10) and Co^{2+} to Co^{3+} (indicated by a notable intensity decrease at 776.9 eV, 778.2 eV, and 778.6 eV accompanied with an intensity increase at 780.2 eV, **Figure S11**). The Ni oxidation is also reflected in the feature at 528.9 eV in the O K-edge spectra of the plasma-treated sample. [62, 63]

Further, N K-edge spectra confirm that nitrogen is implemented into the surface of the plasma-treated sample and suggest the formation of nitride species. However, evaluating the electronic structure of the N species remains challenging because the N K-edge spectrum appears to be distorted due to an intensity modulation induced by a Si_3N_4 window, which is implemented in the setup we used (Figure S11). In addition, it was observed that the intensity of the F K-edge vanishes after plasma treatment. This is in line with EDX results and corroborates the finding of successful removal of the Nafion binder after the plasma treatment (**Figure S13**).

Furthermore, TEY XAS allows us to examine differences in the near-surface electronic structure present after the electrochemical characterization of the material between the plasma-treated and as-prepared Ni-Co-O. The changes in the O K-edge spectra (Figure 10) together with the changes in the Ni and Co L-edge spectra (**Figure S14-S18**) indicate a partial transformation of the Ni-Co-O phase in both samples into a Ni-Co hydroxide phase, as demonstrated by comparison with reference spectra. Along with the structural transformation, the Ni and Co species at the surface of the as-prepared sample become partially oxidized (Figure S11 and Figure S13). This partial oxidation is particularly pronounced for Co.

In contrast, in the plasma-treated sample, in which Ni^{3+} and Co^{3+} contributions were detected, the Ni and Co oxidation states appear to be slightly reduced after applying the electrochemical protocol (Figure S12 and Figure S14). The lower metal oxidation states after electrochemical treatment probably indicate better reversibility of the metal oxidation taking place during OER. This is an indication of structural changes in the active phase and might be correlated with the enhanced Ni/Co-ratio on the surface of the plasma-treated sample observed via XPS. It has to be noted here that the surface sensitivity of XAS in TEY mode is not necessarily identical, although both are in the nm regime. Such compositional changes influence the OER activity [64] and may contribute to the observed differences in electrochemical performance. Most interestingly the Co oxidation state before and post electrochemistry appears more stable in the plasma-treated sample compared to the as-prepared anode, which could be explained by the

lower amount of Co at the surface being stabilized in the bulk, and thus less involvement in the surface reactions.

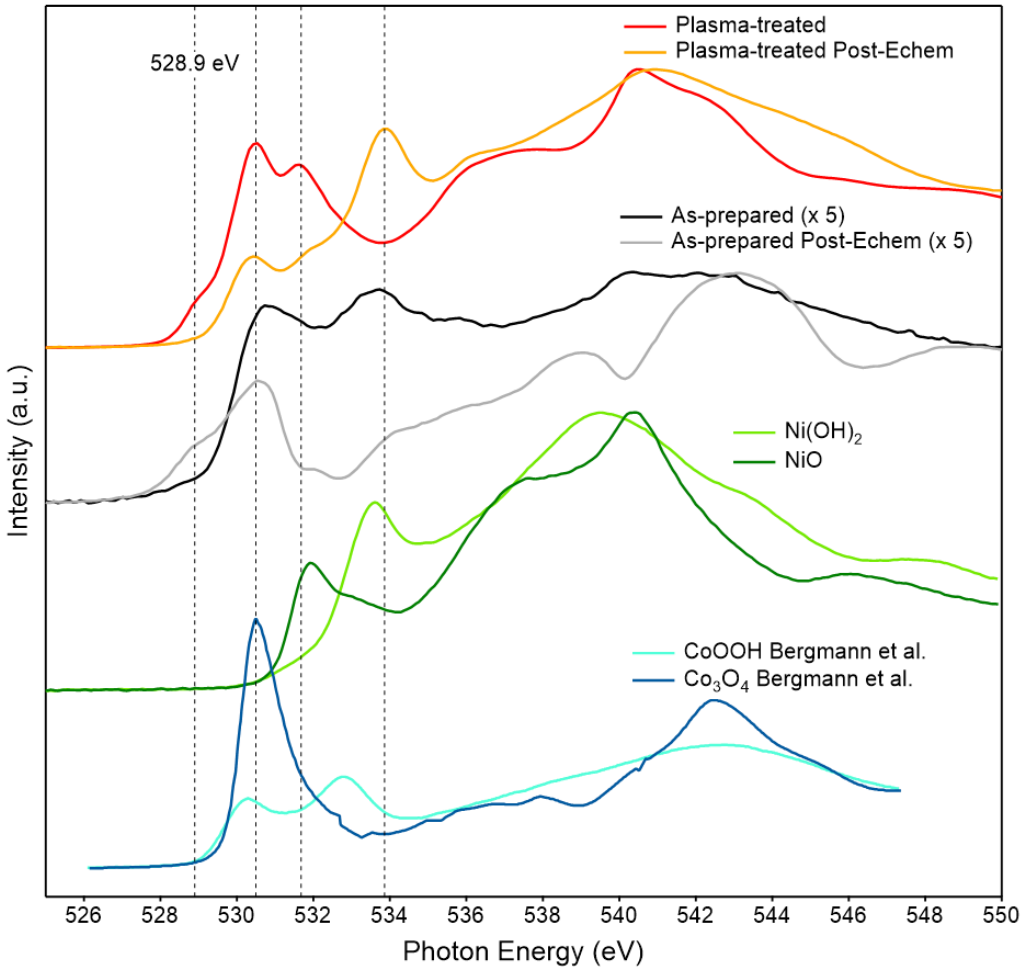

Figure 10 *Averaged O K-edge spectra of the as-prepared and the plasma-treated samples before and after the electrochemical treatment, normalized to their maximum in comparison with reference spectra. The spectra of the as-prepared samples were scaled by a f The literature spectra are taken from Bergmann et al.*[65]*. The vertical lines serve as a guide to the eye to facilitate better comparison of the main spectroscopic features with the reference spectra.*

Another important observation was made at the Fe L-edges, where a small Fe L-edge contribution can be seen only in the spectra of the as-prepared sample indicating some Fe impurities to be present on the surface, which vanished after the plasma treatment (**Figure S18**). After the electrochemical treatment, only apparent oxidation (indicated by the change in the spectral shape) but no obvious changes in the Fe L_3 edge intensity were observed for the as-prepared sample while the Fe signal in the plasma-treated sample showed a strong increase in the Fe signal significantly exceeding that of the as-prepared anode. This indicates a facilitated

Fe-uptake for the plasma-treated Ni-Co-O compared to the as-prepared sample. This is perfectly in line with the observed higher electrocatalytic activity, as the implementation of Fe increased the activity of Ni-Co catalysts severely. [66] The presence of these Fe^{3+} species (Figure **S18** and **S19**) can be attributed to the Fe-containing KOH electrolyte used in our work to mimic application-relevant conditions.

In contrast to the plasma-treated electrode, on which the Nafion was removed by the plasma, the as-prepared electrode still has Nafion present on its surface after the electrochemical treatment, as indicated by the F K-edge spectra (Figure S13). Interestingly, the overall intensity of the F signal even increased after electrochemical treatment, which might originate from the loss of some loosely bound catalyst particles thus exposing more binder. We hypothesize that this Nafion coverage reduces the ECSA, which may also contribute to the lower OER activity of the as-prepared electrode compared to the plasma-treated one. Further, measurement at the N K-edge (Figure S12) clearly shows a partial nitrogen implementation by the N_2 plasma that partly stays in the sample also after the electrochemical treatment. Consequently, we cannot exclude the possibility of nitrogen being implemented in the active phase, probably modifying its activity. Hence, nitrogen implementation may also contribute to the observed performance differences between the plasma-treated and as-prepared anodes.

As the XAS measurements on the as-prepared and plasma-treated Ni-Co-O layers before and after electrochemical tests indicated significant differences as mentioned above, to gain a more dynamic insight into their electrochemical performances, we conducted *operando* Raman measurements. For the *operando* Raman measurements, both samples were first conditioned using a CV protocol (see Experimental section 4.12 for details) before recording the Raman spectra. Raman spectra were then collected at selected potentials based on the features observed from a low scan rate cyclic voltammetry (CV) scan (**Figure S20**) to identify and compare dynamic changes in the active phases in these two electrodes.

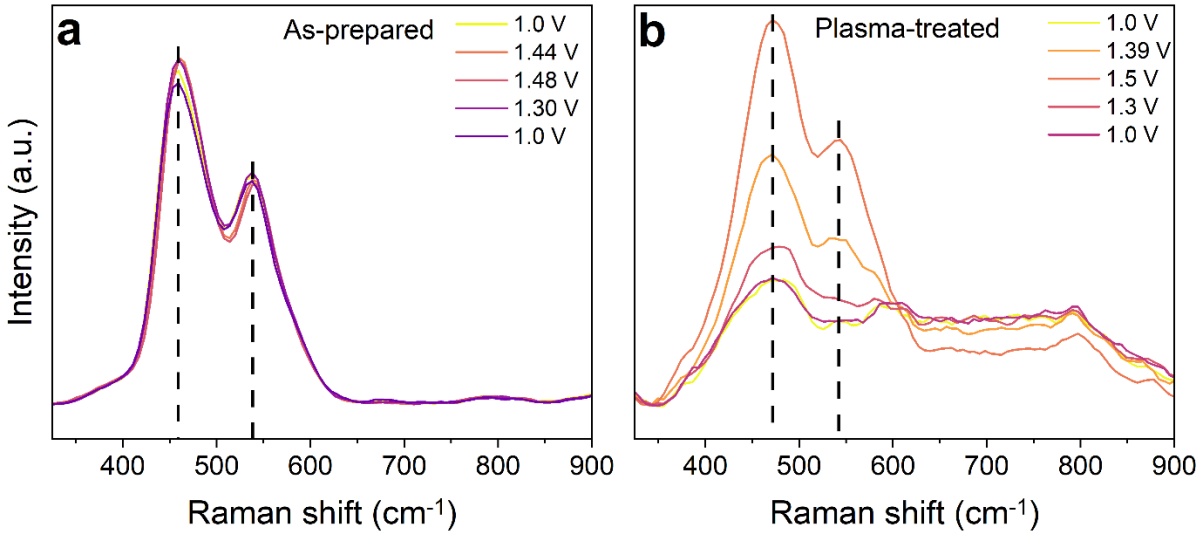

Figure 11 *Operando Raman measurements in 1M KOH on (a) as-prepared and (b) plasma-treated Ni-Co-O layers under constant applied potentials in chronoamperometry measurements. The sequence of applied potentials is shown in the figure legends.*

Figure 11 shows the *operando* Raman measurements conducted on the (a) as-prepared and (b) plasma-treated Ni-Co-O electrodes. Raman spectra of the as-prepared Ni-Co-O layer exhibit two major Raman bands located around 460 and 538 cm^{-1} at an applied potential of 1.0 V vs. RHE which can be assigned to Ni-O vibrations in $Ni(OH)_2$. [67] During the anodic scan, these bands are consistently observed with a small blue shift with increasing the potential up to 1.48 V vs. RHE which is reversible upon applying the reductive potentials. This reproducible blue shift during the anodic scan points to the shortening of the metal-oxygen bond length and thus an increase of the polarizability due to the change of electron cloud distribution within the catalyst layer. [68]

In contrast, after the plasma treatment, there is only a broad Raman band observed starting at 470 cm^{-1} at 1.0 V (Figure 11b). When the potential is stepwise anodically increased, a second peak emerges at 541 cm^{-1} which further increases the intensity at the OER onset potential of 1.5 V. The Raman band at 541 cm^{-1} disappears again during the cathodic scan below 1.3 V. It is reasonable in this case to expect the existence of (oxy-)hydroxy species during OER in these catalysts. It has to be noted, that the potentials were not scanned to a region where OER starts – to avoid interruptions due to bubble formation – and the Raman spectrum of the active phase of the catalyst during OER might still differ from our results. However, Yang et al. reported the broadening of the Ni-OOH species derived from $Ni(OH)_2$ and a shoulder peak along with the 551 cm^{-1} band to the co-existing Ni and Co-OOH in NiCo double hydroxides under applied potentials in 1 M KOH. [69] Similarly, also in our *operando* investigations, a broader nature of

the Raman bands is observed in the plasma-treated electrode compared to the more defined bands observed in the as-prepared Ni-Co-O layer. This suggests that the contribution of different phases varies between the two samples during electrochemical testing or might also result from plasma-induced defects in the crystal structure.

The nitrogen plasma treatment introduces significant structural and chemical modifications to the Ni-Co-O catalyst, enhancing its catalytic performance for OER. Nitrogen plasma likely induces nitrogen doping, leading to the formation of N–M bonds (M = Ni, Co) and oxygen vacancies. These modifications are evidenced by the appearance of the 610 cm^{-1} peak, indicative of partial spinel-like features, and the shift of the 460 cm^{-1} peak, reflecting changes in lattice dynamics possibly due to nitrogen incorporation. Unlike oxygen plasma treatment, which promotes oxidation and formation of fully spinel structures like Co_3O_4, nitrogen plasma enhances the material's conductivity and stability by introducing nitrogen species into the lattice and partial spinel structures. These changes create additional active sites and prevent over-oxidation, as observed by the weak 538 cm^{-1} peak (CoOOH phase). Furthermore, plasma treatment increases the surface area and porosity of the catalyst (Fig. 9c and d), providing greater accessibility to active sites and improving mass transport. In comparison to the pristine material, the plasma-treated catalyst demonstrates enhanced OER activity due to nitrogen doping, which improves electron transport and creates new active sites; defect engineering, which stabilizes catalytic intermediates; and improved stability, which reduces degradation during prolonged OER operation.

Still, an accurate assignment of the Raman bands in each case is rather difficult and the focus is therefore put on the significantly different potentiodynamic behavior of the spectra for the as-prepared and plasma-treated electrodes where the latter shows a prominent reversible phase change and a much more “flexible nature” in comparison to the as-prepared Ni-Co-O under similar applied potentials, which might also be beneficial for activity improvement.

Finally, taking all data together, it is justified to assume that several factors contribute to the enhanced activity of the plasma-treated Ni-Co-O electrodes:

(i) First, the surface morphology of the plasma-treated Ni-Co-O is significantly different from that of the as-prepared layers in such a way that plasma-treatment induces a more homogeneous surface with a larger share of primary particles and thus more surface area that is exposed to the electrolyte.

(ii) Second, the plasma treatment removed most of the organic species from the surface of the electrodes, thus making the active material more accessible to the electrolyte. Both

the more favorable surface morphology and binder removal directly affect the electrochemically active surface area and density of active sites.

(iii) Third, the plasma-treated Ni-Co-O films exhibited a highly hydrophilic surface compared to the hydrophobic nature of the surface in the as-prepared films, due to the changes induced in the surface morphology and removal of surface binder.

(iv) Fourth, XAS studies highlight a higher Fe-uptake by the plasma-treated electrode than the as-prepared Ni-Co-O, together with differences in the surface metal-oxide species between the two types of anodes, and additionally indicate some nitrogen incorporation due to the plasma processing.

(v) Fifth, the Raman features for the plasma-treated samples appear broader compared to the as-prepared samples, indicating the presence of a different phase composition or induced defects in the surface layers.

(vi) Sixth, both XAS and *operando* Raman studies underline a more reversible oxidation behavior in the plasma-treated layers when used as anodes in OER which further influences the activity.

Disentangling the individual effects of each of these phenomena on the OER performance is beyond the scope of this work, however, our findings pave the way for extensive future research in this direction. The coherent workflow for multi-stage anode development enabled this systematic investigation, starting from the micro powder through ink formulation to electrode coating, surface treatment by N_2 plasma, and subsequent application of the electrodes as OER catalysts (**Figure 12**). Finally, the effectiveness of the plasma post-treatment on the OER performance of spray-coated Ni-Co-O is demonstrated as an efficient, potentially scalable way to obtain binder-free, potent anodes, even from commercial materials, by proper processing.

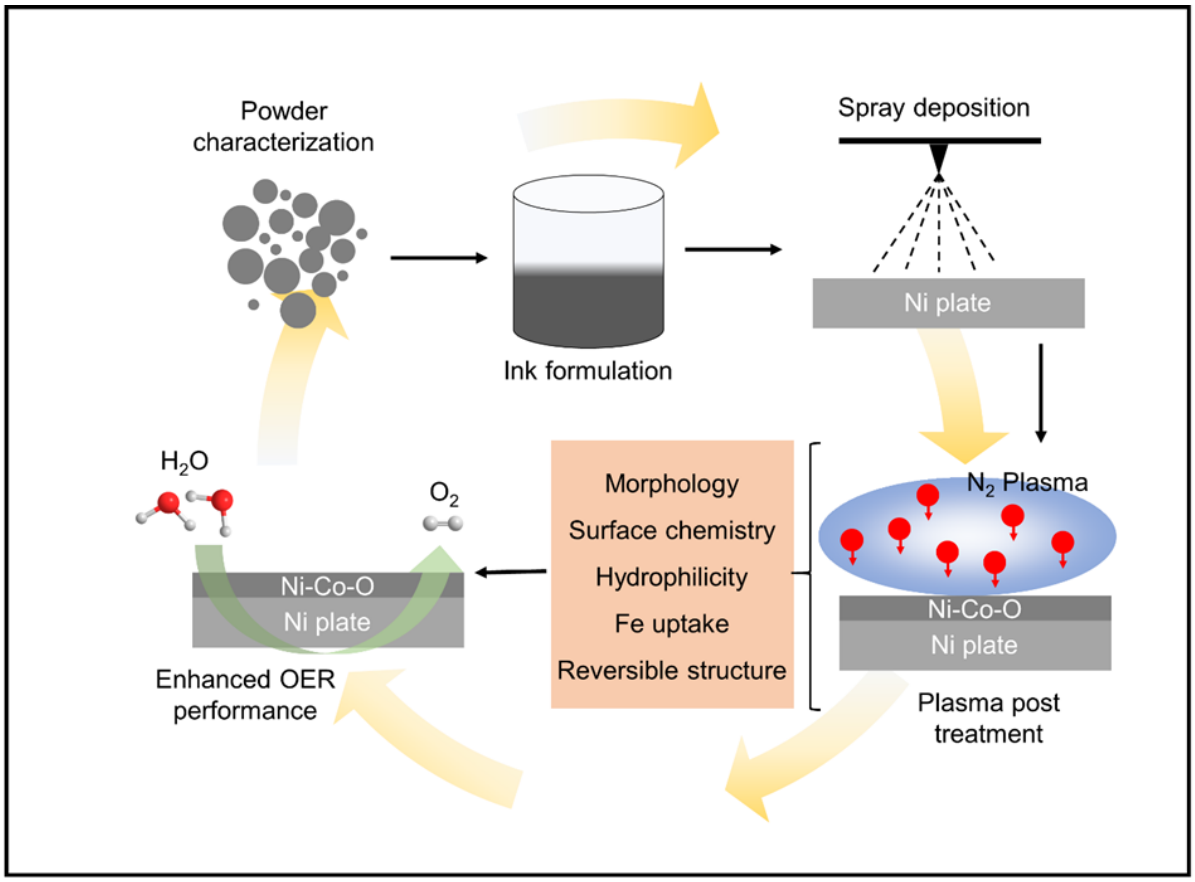

Figure 12 *Schematic representation of the coherent workflow cycle starting from the initial powder selection and characterization through ink formulation, catalyst deposition, and plasma post-treatment-induced changes leading to the observed, significantly enhanced OER performance.*

3. Conclusion

In conclusion, we have demonstrated a systematic approach to characterize transition-metal-oxide catalysts from their initial powder state along the process chain from catalyst inks to coated layers, enabling in-depth understanding, comparability, and a multistage optimization pathway using Ni-Co-O as a model system. At each stage, the material was meticulously analyzed using a comprehensive set of analytical tools, and insights into powder properties, ink formulation, and layer characteristics were leveraged to further refine the system. We chose a commercial Ni-Co-O powder as an example material and first developed a stable catalyst ink by evaluating its Hansen Solubility Parameters. Subsequently, Ni-Co-O films were obtained through spray coating onto Ni plate substrates that were post-processed by means of N_2 plasma to modify the active layer in terms of morphology, pore structure, wettability, and surface

chemistry. The plasma treatment significantly altered the Ni-Co-O films, resulting in a distinct surface morphology and increased accessibility of the active material by removing organic species. The plasma-treated Ni-Co-O layers also exhibited a highly hydrophilic surface, facilitating interaction with the electrolyte. XAS studies indicated a higher Fe uptake from the electrolyte and nitrogen incorporation upon plasma treatment and further pointed to differences in the surface metal-oxide composition, while *operando* Raman studies showed a more reversible oxidation behavior in the plasma-treated layers. Overall, these modifications contributed to an enhanced OER performance of the Ni-Co-O anodes due to the plasma post-treatment with enhanced reproducibility.

The gained, excellent OER performance of the generated anodes underlines the necessity for a thorough continuous characterization of catalysts throughout the entire process chain and highlights the decisive role of plasma post-treatment in further optimizing the anode layer properties. We believe that our approach is easily transferrable to other, similar transition-metal-based systems where material properties can be fine-tuned to achieve high-performing binder-free cost-effective catalysts for alkaline water electrolysis.

4. Experimental Section/Methods

4.1. Materials

Commercial NiO-CoO nanopowder, (99 %, CAS number 58591-45-0) was purchased from Sigma-Aldrich. Deionized water (>18.1 MΩ) was obtained from a Milli-Q system. Nafion™ perfluorosulfonic acid (PFSA) 5 % dispersions – D521, which was used as the binder, was obtained from Ion Power GmbH. For the spray deposition of the Ni-Co-O, nickel plates (Ra<0.1, 99.2 %, HMW Hauner, pre-cut into 1x1 cm^2 pieces) were used as substrates.

4.2. Dispersion preparation and sedimentation analysis

4.2.1. Hansen solubility parameters

Dispersions were obtained by sonicating the Ni-Co-O powder in probe liquids with an ultrasonic homogenizer (Branson). The probe liquids were selected according to the two-step procedure developed by Amin et al. [45]. In the first step, EtOH, DMF, and THF were used to identify liquids that form good dispersions with the Ni-Co-O powder. Based on the stability of the dispersion in the first step, additional probe liquids were screened in the second step and the resulting probe liquids list was used to make the ranking for HSP determination according to Süß et al.[46].

Analytical centrifugation was used to sediment the dispersions using artificial gravity. The dispersions were filled into measurement cells with 2 mm path length and inserted into a LUMisizer LS651 (LUM GmbH) analytical centrifuge and centrifuged at 2000 rpm for 20 h at 20 ^{o}C using 410 nm wavelength light. After the measurement, transmission fingerprints were generated by resolving the measurement time and position. Furthermore, transmittograms were plotted from the sedimentation data as well.

4.2.2. Ink formulation

The catalyst ink was prepared in the following way: first 30 mg of the Ni-Co-O powder was measured into a centrifuge tube followed by the addition of either 30 mL water or 30 mL ethanol: water mixture (volume ratio 1:1 r.t.p). The so-obtained suspension was homogenized by applying 18 minutes of probe sonication (Hielscher UP200Ht, Germany, ultrasonic homogenizer operating at 26 kHz, 20 % amplitude) [37] in three equal intervals of 6 minutes. Before commencing the last round of sonication, a small amount of Nafion (20 wt%) was also added to the mixture. During the probe sonication, the ink was kept inside an ice bath to avoid evaporation.

4.3 Spray coating of Ni-Co-O layers

Ni-Co-O layers were generated by spray coating the Ni-Co-O ink onto Ni plate substrates. Before the spray deposition, nickel plates were cleaned ultrasonically first with de-ionized water, followed by 1 M HCl solution, deionized water, acetone, and isopropanol to remove any surface contaminants. An ultrasonic spray coater (Sono Tek Co., NY) with an air pressure of 30 mbar was used. The Ni plates were heated to 150 °C during spray deposition to facilitate solvent evaporation from the substrate surface. All inks were applied at a constant flow rate of 0.4 mL/min, with a total of 20 layers deposited. To ensure a uniform coating, the first layer was sprayed horizontally across the plate. For subsequent layers, the spray direction was alternated by 90 degrees, with each new layer applied perpendicularly to the previous one. This alternating pattern was repeated until all 20 layers were deposited. Approximately 8 mL of ink was sprayed onto the Ni substrates, resulting in an average catalyst loading of ~120 µg/cm², as confirmed gravimetrically.

4.4. Plasma post-treatment on coated Ni-Co-O layers

After depositing Ni-Co-O films onto Ni plate substrates, the samples underwent a post-treatment in a microwave plasma reactor. The plasma setup used in this work is a custom-built

reactor, specifically designed to incorporate high flexibility in processing capabilities as well as a high adaptability for later scaling and compatibility with industrial applications. A commercially available 2.45 GHz IPLAS CYRANNUS I-6" plasma resonator is used as the basis for the reactor. The samples were positioned on a glass sample holder within the reactor. To eliminate contaminants, the reactor was first evacuated. Nitrogen gas was then introduced into the reactor using mass flow controllers while maintaining the vacuum pump at full speed. A gas flow rate of approximately 400 sccm was carefully adjusted to stabilize the reactor pressure at 1 mbar. With a microwave power set to 1 kW, the plasma was ignited. E-H tuners were employed to achieve the desired plasma mode and to minimize the reflected power. After a treatment duration of 10 min, the plasma treatment was stopped. The gas supply was subsequently shut off, and the reactor was once again evacuated to remove any residual gas. Finally, the reactor was vented, allowing for the safe removal of the treated samples.

4.5. Morphology characterization of Ni-Co-O *powder and films*

4.5.1. TEM- EDX

The morphology, particle size, and elemental distribution of the Ni-Co-O powder were determined using TEM with in-built EDX. TEM-EDX measurements were conducted using a JEOL JEM-2200FS microscope and the sample was obtained by drying an aliquot of the Ni-Co-O micropowder suspended in an organic solvent on a carbon-coated Cu grid under ambient conditions. In addition to the micropowder samples, the morphology of the spray-deposited Ni-Co-O samples as well as plasma-treated Ni-Co-O films was also analyzed by TEM. In this case, the spray-deposited and plasma-treated films were scratched from the Ni substrates followed by suspending them in an organic solvent to obtain a dispersion that could be drop-casted on the TEM grids. The average particle size in each case was determined by measuring at least 200 particles in ImageJ (version 1.54f) software and then fitting the achieved histogram using a log-normal function.

4.5.2. Scanning Electron Microscopy

Morphology of the Ni-Co-O films on the Ni plates was characterized using a Phenom desktop scanning electron microscopy (SEM) from Thermo Fisher Scientific. SEM images were acquired in the secondary electron mode with an acceleration voltage of 15 KeV. The bulk composition of the as-prepared films and after plasma treatment were analyzed using an inbuilt EDX detector in the SEM.

4.5.3. Atomic Force Microscopy

The surface topography of the coated Ni-Co-O layers, both before and after plasma treatment, was further characterized using AFM with the TOSCA 400 (Anton Paar Germany GmbH). In our AFM analysis, we applied multistage data quantification (MSDQ) that we recently developed to accurately extract quantitative and representative surface features. [47] The methodologies and conditions followed in this study are consistent with those outlined in our previous work, and the specific parameters used are detailed in the supporting information, section S1.

4.5.4 Focused ion beam/Scanning electron microscopy

The FIB-SEM analysis was conducted to evaluate the pore structure in the as-prepared and plasma-treated Ni-Co-O films. The catalyst layer on a Ni plate was mounted on an SEM sample holder using copper tape. A Helios NanoLab 600i SEM equipped with a focused ion beam (FIB) was employed for cross-sectional imaging. A protective platinum line (15 µm x 0.5 µm, 0.5 µm thick) was deposited to shield the underlying structure from high-energy FIBs. A rectangular area (15 µm x 15 µm) next to the platinum line was chosen, and a 2 µm deep hole was created using a 6.5 nA FIB beam current. The undamaged wall beneath the platinum deposition was polished with lower current ion beams (up to 93 pA) to achieve a smooth cross-section. Finally, images at various resolutions were captured using SEM. The images obtained were analyzed using an image processing algorithm developed in Matlab (version R2023a). This algorithm processes raw images from the FIB-SEM device, accepting formats such as tiff, jpeg, or png. Initially, the contrast of the image is increased to enhance the pixel intensity difference between the foreground (catalyst particles) and the background (pores). The preprocessed images were then binarized, with black pixels representing catalyst particles and white pixels representing pores. These binary images, essentially data sheets of 1’s and 0’s, are used to determine the porosity. The ratio of white pixels to the total number of pixels corresponds to the porosity or pore coverage of the catalyst layer.

4.5.5. Mercury intrusion porosimetry

The pore size distribution of the catalyst layers was determined using an MIP (Anton Paar Porosimeter 60). For each measurement, 20 pieces of Ni-Co-O catalyst-coated nickel plates, each measuring 0.5 cm by 1 cm, were used. The samples were weighed before the measurements to normalize the volume of mercury intruded, ensuring accurate and consistent data.

4.6. X-ray photoelectron spectroscopy

Surface compositions of the Ni-Co-O films as well as the micropowder feed were determined employing XPS. XPS measurements were conducted employing a custom-designed near ambient pressure (NAP) XPS under ultra-high vacuum (~10^{-8} mbar). The system was equipped with an Al-Kα X-ray source with monochromated X-rays having an energy of 1486.6 eV. The peak deconvolution as well as data analysis was performed using CasaXPS software (version 2.3.26PR1.0). For the peak deconvolution, a Shirley-type background was used. For the XPS analysis of the powder, a small amount was spread on a Cu tape while the spray-deposited films were directly placed on the sample holder using the Cu tape, and a calibration using C1s at 285.0 eV was applied.

4.7. X-ray diffraction

XRD was performed on both the powder and films to evaluate the crystal structure properties. XRD measurements were carried out using a Bruker D8 Advance diffractometer in the Bragg-Brentano reflection mode with Cu Kα radiation (λ = 1.54 Å; 40 kV, 40 mA). For the Ni-Co-O micropowder analysis, particles were suspended in acetone and then drop-casted on a silicon single-crystal sample holder to minimize scattering. Each sample was measured in the2Θ range from 5 to 90° with a step size of 0.01° and a counting time of 1.5 s, resulting in a total measurement time of 3.5 h per sample. Qualitative phase analysis was done by Diffrac. Suite EVA V7.1 (Bruker) with the patterns of Ni (#04-0850), Co (#15-0806), NiO (#65-2901), and CoO (#74-2391) from the ICDD database. Quantitative Rietveld refinement was performed with the software TOPAS 7.0 (Bruker) to calculate the lattice parameters and crystallite sizes.

4.8. Raman spectroscopy

Micro Raman analysis was used to explore the vibrational modes of the powder and film samples. Raman analysis was conducted using a Thermo Scientific micro Raman instrument

(make and model) equipped with a 532 nm excitation laser. However, for the analysis of the Ni-Co-O powder sample, 783 nm laser excitation was used.

4.9 Contact angle measurements

Contact Angle Measurements of the as-prepared and plasma-treated Ni-Co-O layers were conducted employing OCA15PRO equipment (Data Physics Instruments GmbH). The measurements were carried out with 1 M KOH as the liquid which was dropped at a drop-eject-rate of 5µL s^{-1} with simultaneous capturing of the image from which the contact angles were determined.

4.10 Electrochemical OER using Ni-Co-O *films as anodes*

Ni plates coated with Ni-Co-O layers were tested with and without plasma-treatment for their electrochemical performance by using them as anodes for the alkaline OER in both flow cell and beaker cell setups.

4.10.1 Beaker cell electrochemical measurements

Figure S21 shows the electrochemical protocol used in the beaker cell setup. In brief, the electrodes were first electrochemically conditioned, by 50 CVs from 0.2-1.45 V vs. RHE with a scan rate of 100 mV s^{-1}. Afterward, the initial OER activity is determined with 3 CVs from 1-1.8 V vs. RHE at a scan rate of 5 mV s^{-1}. In the next step, the short-term stability of the samples is determined by a CP measurement at 100 mA cm^{-2} for 2 h. The final OER activity is determined with the same parameters as the initial activity. Before every protocol step, an electrochemical impedance spectrum (300 kHz- 1 kHz @OCP with 10 mV rms AC voltage) was obtained to determine the uncompensated resistance. If not stated otherwise, all potentials are corrected for 100 % with the real impedance value obtained where the phase angle reaches its value closest to zero. The measurements were performed at room temperature in 1 M KOH with a controlled iron concentration of 15 ppb and 110 ppb. For all materials, a triple determination was performed.

4.10.2 Flow cell electrochemical measurements

The flow cell setup to conduct OER experiments consisted of a two-compartment batch electrochemical reactor made of PEEK with flow recirculation. This setup was chosen to closely mimic the conditions encountered in practical applications (**Figure S22**). The electrode compartments were separated by an anion exchange membrane (Fumatech fumasep FAA-3-

PK-130, Quintech), which was activated in 1 M KOH at least 24 h before the experiment. We used Ni-foam as a counter electrode (99.9 % purity, GoodFellow) and an Ag/AgCl (3.4 M KCl) leak-free reference electrode (Innovative Instruments, Inc.). The working electrode was the electrode to be tested, with a 0.95 cm^2 geometric area exposed to the electrolyte. The electrolyte was 1 M KOH, prepared with KOH pellets (85 % purity, Sigma Aldrich) in ultrapure water (MilliQ, 18.2 MΩ cm). The electrolyte was recirculated from separate reservoirs through the anode and cathode compartments at a constant flow rate of 9 mL min^{-1} by a peristaltic pump (Minipulse 3 Gilson). N_2 gas (99.995 %) was bubbling in both compartments during the measurements.

We used a Metrohm Autolab potentiostat/galvanostat PGSTAT204 for the electrochemical measurements. The electrochemical program applied comprised seven steps:

1) Potentiostatic Electrochemical Impedance Spectroscopy (PEIS) measured at open-circuit potential (OCP) in a frequency range from 100 kHz to 1 Hz using 10 mV amplitude.

2) Conditioning of the electrode surface by registering 50 cyclic voltammograms (CV) at 100 mV s^{-1} within the potential window from 0.2 to 1.47 V vs RHE.

3) Three CVs between 1 and 1.8 V vs RHE at 5 mV s^{-1}.

4) PEIS at OCP.

5) Chronopotentiometry (CP) at 100 mA cm^{-2} for 2 h.

6) PEIS at OCP.

7) Three CVs between 1 and 1.8 V vs RHE at 5 mV s^{-1}.

For each electrode, all the measurements were conducted in triplicate. The recorded potentials were converted from Ag/AgCl (3 M KCl) scale to the reversible hydrogen electrode (RHE) scale using equations (1) and (2) [70, 71]:

$$E_{RHE} = E_{measured} + E0_{Ag/AgCl} + 0.059\ pH - i \cdot Ru \quad (1)$$

$$pH = 14 + \log([OH^-]) + \log(\gamma) \quad (2)$$

E_{RHE}: Working electrode potential vs. RHE (V) corrected 100 % manually for ohmic drop, $E_{measured}$: Measured potential at the working electrode vs. Ag/AgCl (3 M KCl), E_0Ag/AgCl: Formal potential of Ag/AgCl (3 M KCl) vs. RHE (0.207 V), pH: pH value determined considering the OH^- concentration and the activity coefficient of KOH in water (γ = 0.766), i: current in Amperes, Ru: Uncompensated resistance in Ohms, measured at high frequencies in the Nyquist plots built with PEIS data.

4.11 X-ray absorption spectroscopy

The XAS measurements were conducted in the near-ambient pressure XPS end station [72] connected to the ISISS beamline at the BESSY II synchrotron radiation facility. The chamber was operated at high vacuum conditions, while the total electron yield (TEY) signal was collected on the analyzer nozzle, and the total fluorescence yield (TFY) signal was measured by a photodiode. Two individual spectra were recorded on each spot, and two different spots were measured on each sample. If not differently stated, the averaged spectra of these individual measurements are shown. The spectra were divided by the mirror current to correct for flux differences along the edge and a linear background was subtracted. The NiO and $Ni(OH)_2$ reference spectra were recorded with an equivalent strategy at the LiXEdrom experimental station attached to the U49-2 PGM-1 beamline at the BESSY II synchrotron facility [73].

4.12 Operando Raman spectroscopy

Operando Raman measurements were performed using a commercial in situ Raman cell obtained from the online platform redox.me coupled with Raman spectroscopy from Oceanview with an excitation wavelength of 532 nm. The as-prepared and plasma-treated Ni-Co-O/Ni electrodes were used as the working electrode, Pt wire as the counter, and Ag/AgCl as the reference electrode in a three-electrode set-up. The electrodes were preconditioned for 300 CVs in 1 M KOH before the recording of the Raman spectra. Afterward, a few CVs with lower scan rates were conducted to choose the potentials for the chronoamperometry measurements during which Raman spectra were collected. Each potential was applied for 6 minutes, and Raman spectra were simultaneously recorded with an integration time of 1 minute in each case.

Supporting Information

Supporting Information is available from the Wiley Online Library or the author.

Acknowledgments

The authors acknowledge the financial support from the Federal Ministry of Education and Research for the PrometH2eus project within the H2Giga framework (funding numbers 03HY105F, 03HY105E, 03HY105A). We are also grateful for the support provided by the Mercator Research Center Ruhr (MERCUR.Exzellenz, 'DIMENSION' Ex-2021-0034). This work was also funded by the UDE Postdoc Seed Funding. IS and CA acknowledge the support of the Ministry of Culture and Science of the State of North Rhine-Westphalia (PB22-019).

Open Access funding was facilitated and organized by Projekt DEAL. We extend our thanks to M. Heidelmann from the Interdisciplinary Center for Analytics on the Nanoscale (ICAN) for their valuable assistance. John-Tommes Krzeslack, Lukas Pielsticker, and Walid Hetaba from MPI-CEC are greatly acknowledged for their support of the XPS analysis. XAS Measurements were carried out at the ISSIS beamline and the LiXEdrom endstation at the U49-2 PGM-1 beamline, both allocated at the BESSY II electron storage ring operated by the Helmholtz-Zentrum Berlin für Materialien und Energie.

Received: ((will be filled in by the editorial staff))
Revised: ((will be filled in by the editorial staff))
Published online: ((will be filled in by the editorial staff))

References

1. Tüysüz, H., *Alkaline Water Electrolysis for Green Hydrogen Production.* Accounts of Chemical Research, 2024: p. 697-710.
2. Zuo, Y., et al., *High-performance alkaline water electrolyzers based on Ru-perturbed Cu nanoplatelets cathode.* Nature Communications, 2023. **14**(1): p. 4680.
3. Chatenet, M., et al., *Water electrolysis: from textbook knowledge to the latest scientific strategies and industrial developments.* Chemical Society Reviews, 2022. **51**(11): p. 4583-4762.
4. Zhang, Y.-C., et al., *NiCo-based electrocatalysts for the alkaline oxygen evolution reaction: a review.* Acs Catalysis, 2021. **11**(20): p. 12485-12509.
5. Yue, M., et al., *Hydrogen energy systems: A critical review of technologies, applications, trends and challenges.* Renewable and Sustainable Energy Reviews, 2021. **146**: p. 111180.
6. Wang, Q., et al., *Long‐term stability challenges and opportunities in acidic oxygen evolution electrocatalysis.* Angewandte Chemie, 2023. **135**(11): p. e202216645.
7. Xu, Z.J., *Transition metal oxides for water oxidation: All about oxyhydroxides?* Science China Materials, 2019. **63**(1): p. 3-7.
8. Wen, N., et al., *Electrocatalysts for the oxygen evolution reaction: mechanism, innovative strategies, and beyond.* Materials Chemistry Frontiers, 2023. **7**(20): p. 4833-4864.
9. Higareda, A., et al., *Advanced Electrocatalysts for the Oxygen Evolution Reaction: From Single-to Multielement Materials.* Catalysts, 2023. **13**(10): p. 1346.
10. Plevova, M., J. Hnat, and K. Bouzek, *Electrocatalysts for the oxygen evolution reaction in alkaline and neutral media. A comparative review.* Journal of Power Sources, 2021. **507**: p. 230072.
11. Jamesh, M.-I. and X. Sun, *Recent progress on earth abundant electrocatalysts for oxygen evolution reaction (OER) in alkaline medium to achieve efficient water splitting–A review.* Journal of Power Sources, 2018. **400**: p. 31-68.

12. Xie, X., et al., *Oxygen evolution reaction in alkaline environment: material challenges and solutions.* Advanced Functional Materials, 2022. **32**(21): p. 2110036.
13. Cherevko, S., et al., *Oxygen and hydrogen evolution reactions on Ru, RuO2, Ir, and IrO2 thin film electrodes in acidic and alkaline electrolytes: A comparative study on activity and stability.* Catalysis Today, 2016. **262**: p. 170-180.
14. Sun, H. and W. Jung, *Recent advances in doped ruthenium oxides as high-efficiency electrocatalysts for the oxygen evolution reaction.* Journal of Materials Chemistry A, 2021. **9**(28): p. 15506-15521.
15. Lee, Y., et al., *Synthesis and activities of rutile IrO2 and RuO2 nanoparticles for oxygen evolution in acid and alkaline solutions.* The journal of physical chemistry letters, 2012. **3**(3): p. 399-404.
16. Audichon, T., et al., *IrO2 coated on RuO2 as efficient and stable electroactive nanocatalysts for electrochemical water splitting.* The Journal of Physical Chemistry C, 2016. **120**(5): p. 2562-2573.
17. Tan, D., et al., *Recent progress in noble-metal-free electrocatalysts for alkaline oxygen evolution reaction.* Frontiers in Chemistry, 2022. **10**: p. 1071274.
18. Chen, X., et al., *Research advances in earth-abundant-element-based electrocatalysts for oxygen evolution reaction and oxygen reduction reaction.* 2023.
19. Wang, S., A. Lu, and C.-J. Zhong, *Hydrogen production from water electrolysis: role of catalysts.* Nano Convergence, 2021. **8**(1): p. 4.
20. Han, N., et al., *Designing oxide catalysts for oxygen electrocatalysis: insights from mechanism to application.* Nano-Micro Letters, 2023. **15**(1): p. 185.
21. Raveendran, A., M. Chandran, and R. Dhanusuraman, *A comprehensive review on the electrochemical parameters and recent material development of electrochemical water splitting electrocatalysts.* RSC advances, 2023. **13**(6): p. 3843-3876.
22. Zhou, Y., et al., *Boosting oxygen electrocatalytic activity of Fe–N–C catalysts by phosphorus incorporation.* Journal of the American Chemical Society, 2023. **145**(6): p. 3647-3655.
23. Vazhayil, A., et al., *A comprehensive review on the recent developments in transition metal-based electrocatalysts for oxygen evolution reaction.* Applied surface science advances, 2021. **6**: p. 100184.
24. Chen, X., et al., *Recent advances in earth-abundant first-row transition metal (Fe, Co and Ni)-based electrocatalysts for the oxygen evolution reaction.* Energy Materials, 2022. **2**(4): p. 200028.
25. Gong, M. and H. Dai, *A mini review of NiFe-based materials as highly active oxygen evolution reaction electrocatalysts.* Nano Research, 2015. **8**: p. 23-39.
26. Tareen, A.K., et al., *Nickel‐based transition metal nitride electrocatalysts for the oxygen evolution reaction.* ChemSusChem, 2019. **12**(17): p. 3941-3954.
27. Liu, X.-H., et al., *Recent advances in nickel-based catalysts for electrochemical reduction of carbon dioxide.* Advanced Sensor and Energy Materials, 2023: p. 100073.
28. Lakhan, M.N., et al., *Transition Metals-Based Electrocatalysts for Alkaline Overall Water Splitting: Advancements, Challenges, and Perspectives.* Chemical Communications, 2024.
29. Sheng, H., et al., *Metal-compound-based electrocatalysts for hydrogen peroxide electrosynthesis and the electro-Fenton process.* ACS Energy Letters, 2022. **8**(1): p. 196-212.
30. Li, Y., et al., *Ni/Co-based nanosheet arrays for efficient oxygen evolution reaction.* Nano Energy, 2018. **52**: p. 360-368.
31. López-Fernández, E., et al., *Recent advances in alkaline exchange membrane water electrolysis and electrode manufacturing.* Molecules, 2021. **26**(21): p. 6326.

32. Gerschel, P., et al., *Determining materials for energy conversion across scales: The alkaline oxygen evolution reaction.* Carbon Energy, 2024: p. e608.
33. Sudalai Muthu, K. and P. Perumal, *Synthesis and characterization of NiO Nanoparticles using egg white method.* Journal of Materials Science: Materials in Electronics, 2017. **28**(13): p. 9612-9617.
34. Kuang, T., et al., *Controlled synthesis of cobalt nanocrystals on the carbon spheres for enhancing Fischer–Tropsch synthesis performance.* Journal of energy chemistry, 2019. **33**: p. 67-73.
35. Bhandari, S., et al., *Exploring the Effect of Ball Milling on the Physicochemical Properties and Oxygen Evolution Reaction Activity of Nickel and Cobalt Oxides.* Advanced Energy and Sustainability Research. **n/a**(n/a): p. 2400183.
36. Qiu, Y., et al., *Pseudocapacitive behaviors of mesoporous nickel–cobalt oxide nanoplate electrodes in different electrolyte systems.* New Journal of Chemistry, 2017. **41**(5): p. 2124-2130.
37. Vegard, L., *Die konstitution der mischkristalle und die raumfüllung der atome.* Zeitschrift für Physik, 1921. **5**(1): p. 17-26.
38. Kuboon, S. and Y.H. Hu, *Study of NiO− CoO and Co3O4− Ni3O4 solid solutions in multiphase Ni− Co− O systems.* Industrial & engineering chemistry research, 2011. **50**(4): p. 2015-2020.
39. Wang, J., et al., *Electrospinning Synthesis of Porous NiCoO2 Nanofibers as High‐Performance Anode for Lithium‐Ion Batteries.* Particle & Particle Systems Characterization, 2019. **36**(7): p. 1900109.
40. Chastain, J. and R.C. King Jr, *Handbook of X-ray photoelectron spectroscopy.* Perkin-Elmer Corporation, 1992. **40**: p. 221.
41. Ehsan, M.A., A.S. Hakeem, and A. Rehman, *Hierarchical growth of CoO nanoflower thin films influencing the electrocatalytic oxygen evolution reaction.* Electrocatalysis, 2020. **11**: p. 282-291.
42. van Limpt, R.T., et al., *Unraveling the Role of the Stoichiometry of Atomic Layer Deposited Nickel Cobalt Oxides on the Oxygen Evolution Reaction.* Advanced Science, 2024: p. 2405188.
43. Anwar, O., et al., *Hansen parameter evaluation for the characterization of titania photocatalysts using particle size distributions and combinatorics.* Nanoscale, 2022. **14**(37): p. 13593-13607.
44. Bapat, S., et al., *Towards a framework for evaluating and reporting Hansen solubility parameters: applications to particle dispersions.* Nanoscale advances, 2021. **3**(15): p. 4400-4410.
45. Amin, A.S., et al., *A Procedure for Rational Probe Liquids Selection to Determine Hansen Solubility Parameters.* ChemCatChem, 2024. **16**(6): p. e202301393.
46. Süß, S., et al., *Determination of Hansen parameters for particles: A standardized routine based on analytical centrifugation.* Advanced Powder Technology, 2018. **29**(7): p. 1550-1561.
47. Jain, A., et al., *From Small‐Area Observations to Insight: Surface‐Feature‐Extrapolation of Anodes for Alkaline Oxygen Evolution Reaction.* ChemCatChem, 2024. **16**(5): p. e202301461.
48. Kräenbring, M.-A., F. Özcan, and D. Segets, *Analyzing Emulsion Dynamics via Direct Visualization and Statistical Methodologies.* ACS omega, 2024. **9**(37): p. 39253-39258.
49. Jain, A., et al., *A Proof-of-Principle Demonstration: Exploring the Effect of Anode Layer Microstructure on the Alkaline Oxygen Evolution Reaction.*

50. Pham, N.P., J.N. Burghartz, and P.M. Sarro, *Spray coating of photoresist for pattern transfer on high topography surfaces.* Journal of Micromechanics and Microengineering, 2005. **15**(4): p. 691.
51. Wang, F.-H., et al., *Influence of hydrogen plasma treatment on Al-doped ZnO thin films for amorphous silicon thin film solar cells.* Current Applied Physics, 2011. **11**(1): p. S12-S16.
52. Lim, T., et al., *Surface modification of oxide nanowires by nitrogen plasma.* Electrochemical and Solid-State Letters, 2011. **14**(5): p. H218.
53. Kong, X., et al., *Plasma-assisted synthesis of nickel-cobalt nitride–oxide hybrids for high-efficiency electrochemical hydrogen evolution.* Materials Today Energy, 2021. **21**: p. 100784.
54. Qi, J., W. Zhang, and R. Cao, *Porous materials as highly efficient electrocatalysts for the oxygen evolution reaction.* ChemCatChem, 2018. **10**(6): p. 1206-1220.
55. Ghosh, S., et al., *Microstructural pore analysis of the catalyst layer in a polymer electrolyte membrane fuel cell: a combination of resin pore-filling and FIB/SEM.* International Journal of Hydrogen Energy, 2015. **40**(45): p. 15663-15671.
56. Zhou, B., et al., *Surface design strategy of catalysts for water electrolysis.* Small, 2022. **18**(27): p. 2202336.
57. Gohlke, C., et al., *Boosting the Oxygen Evolution Reaction Performance of Ni‐Fe‐Electrodes by Tailored Conditioning.* ChemElectroChem, 2024. **11**(18): p. e202400318.
58. Le Formal, F., et al., *Influence of composition on performance in metallic iron–nickel–cobalt ternary anodes for alkaline water electrolysis.* Acs Catalysis, 2020. **10**(20): p. 12139-12147.
59. Lyons, M., et al., *Hydrous nickel oxide: redox switching and the oxygen evolution reaction in aqueous alkaline solution.* Journal of The Electrochemical Society, 2012. **159**(12): p. H932.
60. Mattinen, M., et al., *Dynamics of precatalyst conversion and iron incorporation in nickel-based alkaline oxygen evolution reaction catalysts.* Cell Reports Physical Science, 2024.
61. McCrory, C.C., et al., *Benchmarking heterogeneous electrocatalysts for the oxygen evolution reaction.* Journal of the American Chemical Society, 2013. **135**(45): p. 16977-16987.
62. Yoshida, M., et al., *Direct observation of active nickel oxide cluster in nickel–borate electrocatalyst for water oxidation by in situ O K-edge X-ray absorption spectroscopy.* The Journal of Physical Chemistry C, 2015. **119**(33): p. 19279-19286.
63. Tesch, M.F., et al., *Vacuum compatible flow-cell for high-quality in situ and operando soft X-ray photon-in–photon-out spectroelectrochemical studies of energy materials.* Electrochemical Science Advances, 2022. **2**(6): p. e2100141.
64. Krivina, R.A., et al., *Oxygen electrocatalysis on mixed-metal oxides/oxyhydroxides: from fundamentals to membrane electrolyzer technology.* Accounts of Materials Research, 2021. **2**(7): p. 548-558.
65. Bergmann, A., et al., *Unified structural motifs of the catalytically active state of Co (oxyhydr) oxides during the electrochemical oxygen evolution reaction.* Nature Catalysis, 2018. **1**(9): p. 711-719.
66. Stevens, M.B., et al., *Ternary Ni-Co-Fe oxyhydroxide oxygen evolution catalysts: Intrinsic activity trends, electrical conductivity, and electronic band structure.* Nano Research, 2019. **12**: p. 2288-2295.
67. Wu, Y., et al., *Tracking the structural evolution and activity origin of Co-doped NiFe layered double hydroxide for enhanced oxygen evolution reaction.* Chemical Engineering Journal, 2024. **488**: p. 151086.

68. Chen, D., et al., *Probing structural evolution and charge storage mechanism of NiO2Hx electrode materials using in operando resonance Raman spectroscopy.* Advanced Science, 2016. **3**(6).
69. Yang, X., et al., *An unveiled electrocatalysis essence of NiCo hydroxides through in situ Raman spectroscopy for urea oxidation.* Energy Technology, 2022. **10**(5): p. 2101010.
70. Braun, M., et al., *Electrooxidation of alcohols on mixed copper–cobalt hydroxycarbonates in alkaline solution.* ChemElectroChem, 2022. **9**(13): p. e202200267.
71. Radha, A., et al., *The Effect of Interlayer Anion Grafting on Water Oxidation Electrocatalysis: A Comparative Study of Ni‐and Co‐Based Brucite‐Type Layered Hydroxides, Layered Double Hydroxides and Hydroxynitrate Salts.* Chemistry‐A European Journal, 2021. **27**(68): p. 16930-16937.
72. Knop‐Gericke, A., et al., *X‐Ray photoelectron spectroscopy for investigation of heterogeneous catalytic processes.* Advances in catalysis, 2009. **52**: p. 213-272.
73. Aziz, E.F., et al., *LiXEdrom: high energy resolution RIXS station dedicated to Liquid Investigation at BESSY II.* Journal of large-scale research facilities JLSRF, 2016. **2**: p. A80-A80.

We present a coherent workflow for Ni-Co-O anode optimization in alkaline oxygen evolution (OER) reaction covering the entire process chain, integrating ink optimization, layer development, and plasma post-processing. Plasma treatment enhanced surface morphology, porosity, wettability, redox reversibility, and Fe uptake, thus overall enhancing the OER performance compared to the as-prepared layers.

Vineetha Vinayakumar*, Timo Wagner, Christian Marcks, Jacob Johny, Garlef Wartner, Marc F. Tesch, Ioannis Spanos, Aliakbar Ghafari, Adarsh Jain, Oleg Prymak, Ignacio Sanjuán, Ahammed Suhail Odungat, Osama Anwar, Mohit Chatwani, Aneeta Jose, Vimanshu Chanda, Axel Knop-Gericke, Corina Andronescu, Anna K Mechler, Nicolas Wöhrl, and Doris Segets*

Ni-Co-O anodes for the alkaline oxygen evolution reaction: Multistage electrode optimization and plasma-assisted activity enhancement enabled by a coherent workflow

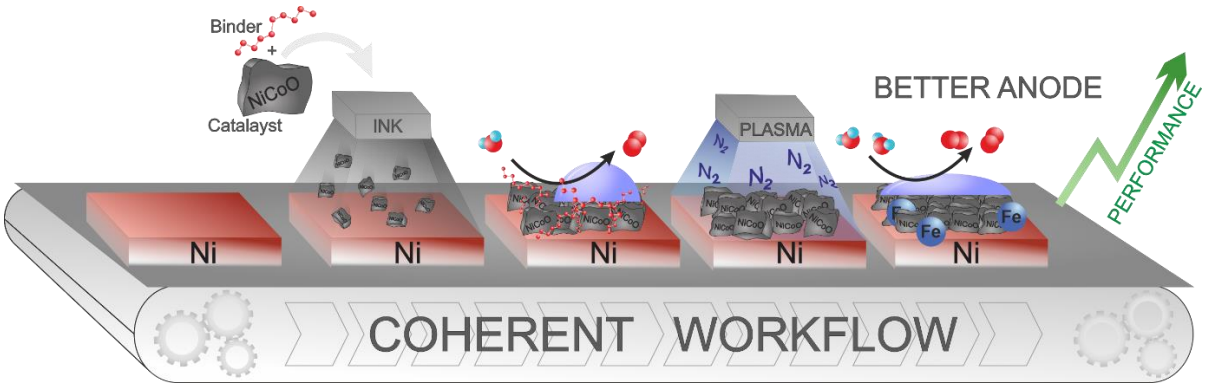

Supporting Information

Ni-Co-O anodes for the alkaline oxygen evolution reaction: Multistage electrode optimization and plasma-assisted activity enhancement enabled by a coherent workflow

Vineetha Vinayakumar, Timo Wagner, Christian Marcks, Jacob Johny, Garlef Wartner, Marc F. Tesch, Ioannis Spanos, Aliakbar Ghafari, Adarsh Jain, Oleg Prymak, Ignacio Sanjuán, Ahammed Suhail Odungat, Osama Anwar, Mohit Chatwani, Aneeta Jose, Vimanshu Chanda, Axel Knop-Gericke, Corina Andronescu, Anna K Mechler, Nicolas Wöhrl, and Doris Segets**

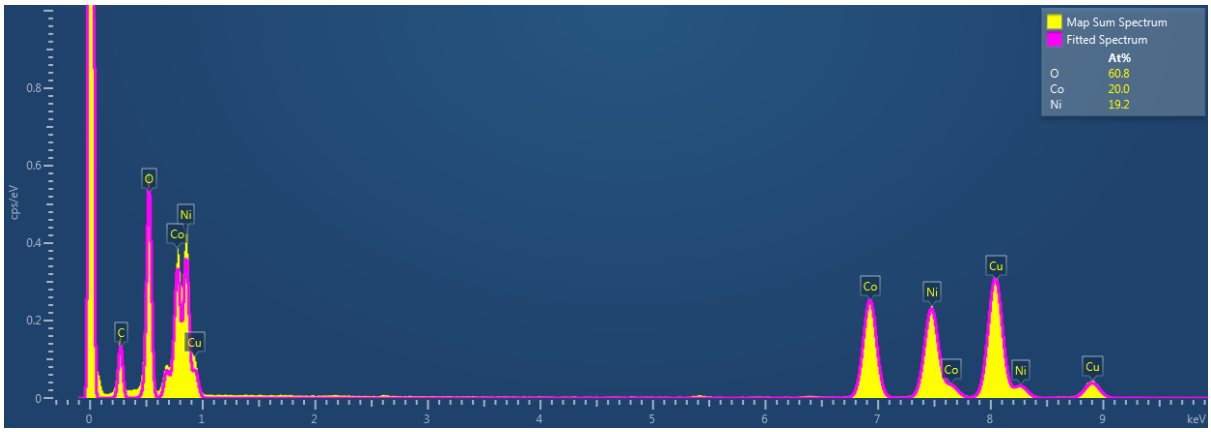

Figure S1 EDX data of the commercial Ni-Co-O powder.

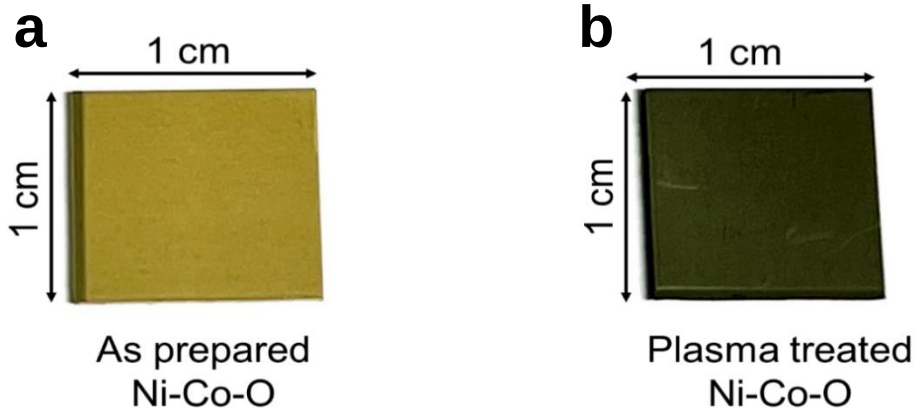

Figure S2 Photographs showing the (a) as-prepared and (b) plasma-treated Ni-Co-O films deposited on Ni plate substrates.

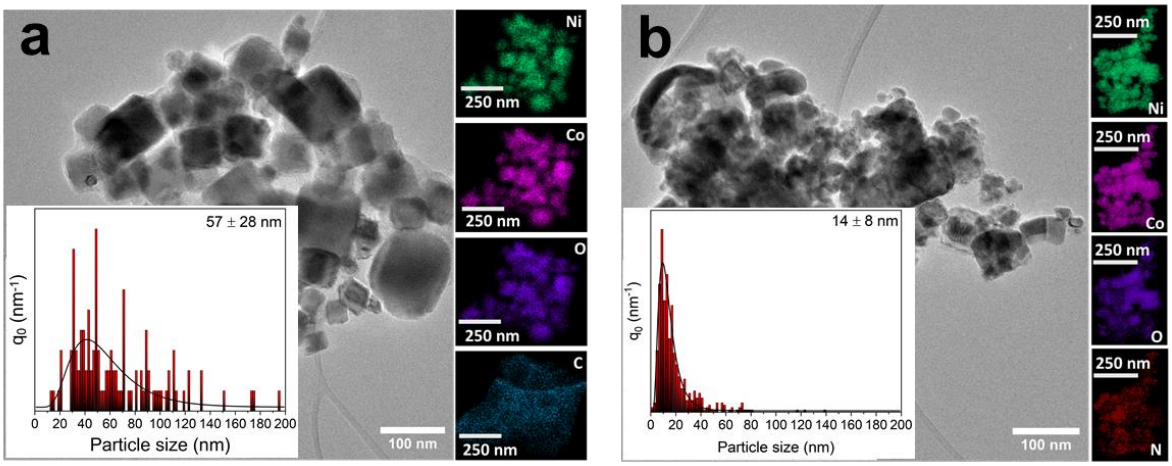

Figure S3 TEM characterization of the (a) as-prepared and (b) plasma-treated Ni-Co-O films with particle size distributions in the inset and respective EDX mappings showing the distribution of the elements within the particles.

Table ST1 Parameters utilized in the primary AFM study.

Parameters	AP	PT
$H_{s\,(ROS1)}$ /-	0.8707	0.8842
$H_{s\,(ROS2)}$ /-	0.8588	0.8290
$H_{s\,(ROS3)}$ /-	0.8075	0.8651
$H_{s\,(ROS4)}$ /-	0.8786	0.8438
σ /-	0.032	0.024
E /%	2.5	2.5
α /%	95 %	95 %
x_z /-	7	4
x /-	10	10

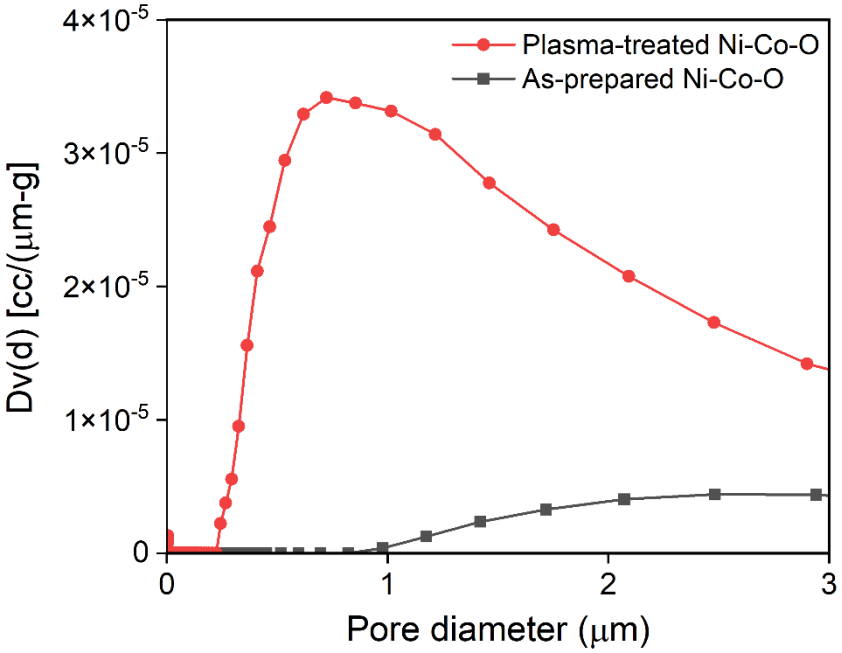

Figure S4 Pore size distribution of as-prepared and plasma-treated Ni-Co-O anodes on Ni substrate derived from mercury intrusion porosimetry (MIP)

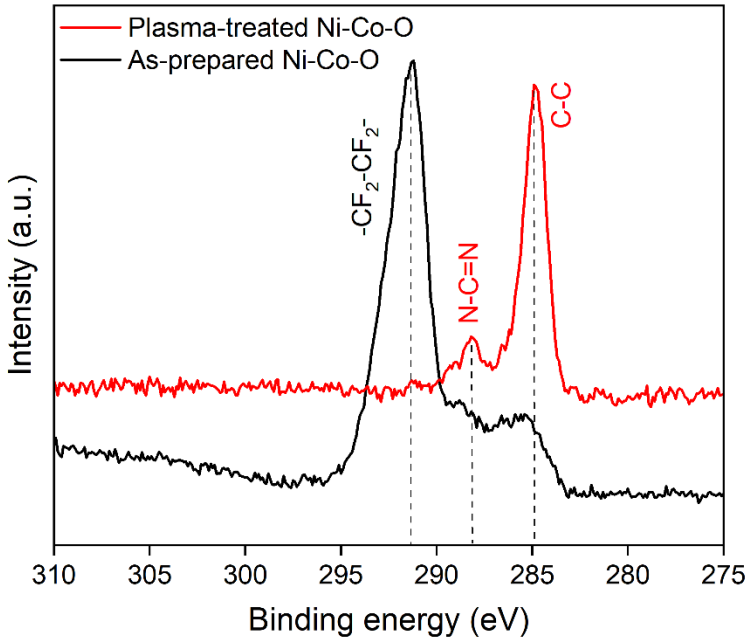

Figure S5 High-resolution C1s XPS spectra of as-prepared and plasma-treated Ni-Co-O layers.

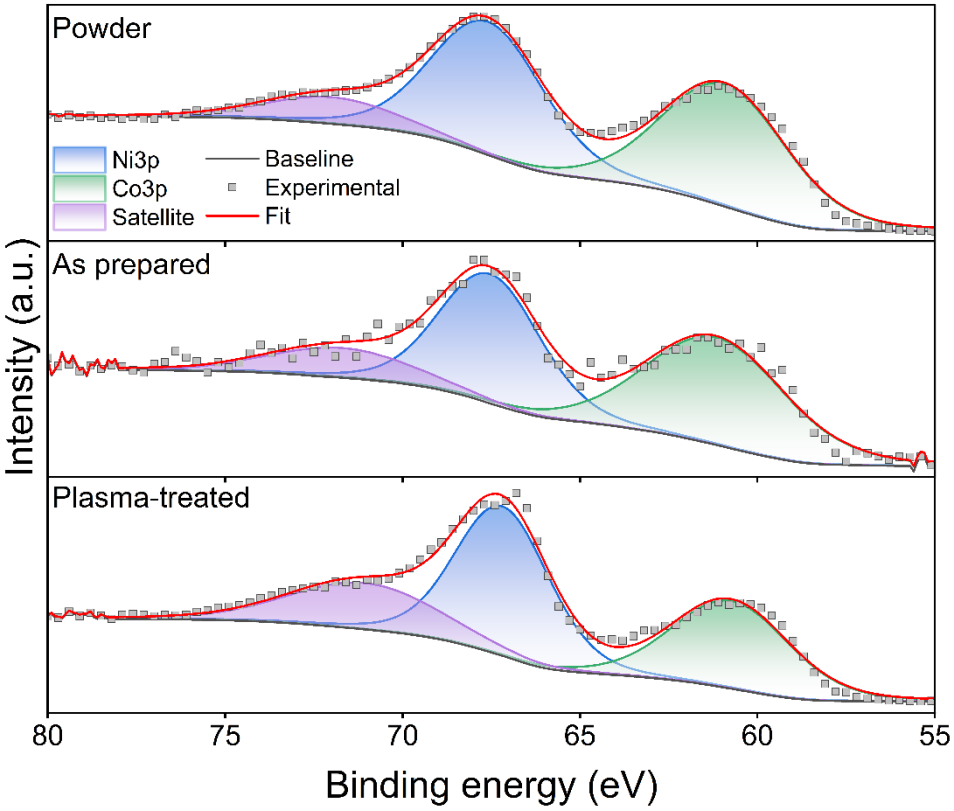

Figure S6 XPS high-resolution spectra showing the Ni3p and Co3p regions in the Ni-Co-O powder, as prepared and plasma-treated films.

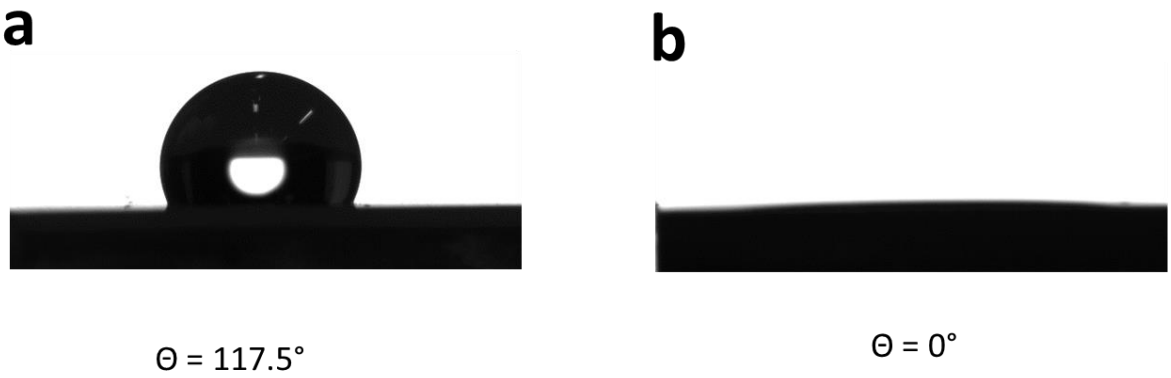

Figure S7 Contact angle measurements performed on the (a) as-prepared and (b) plasma-treated Ni-Co-O films showing hydrophilic surface after the plasma treatment.

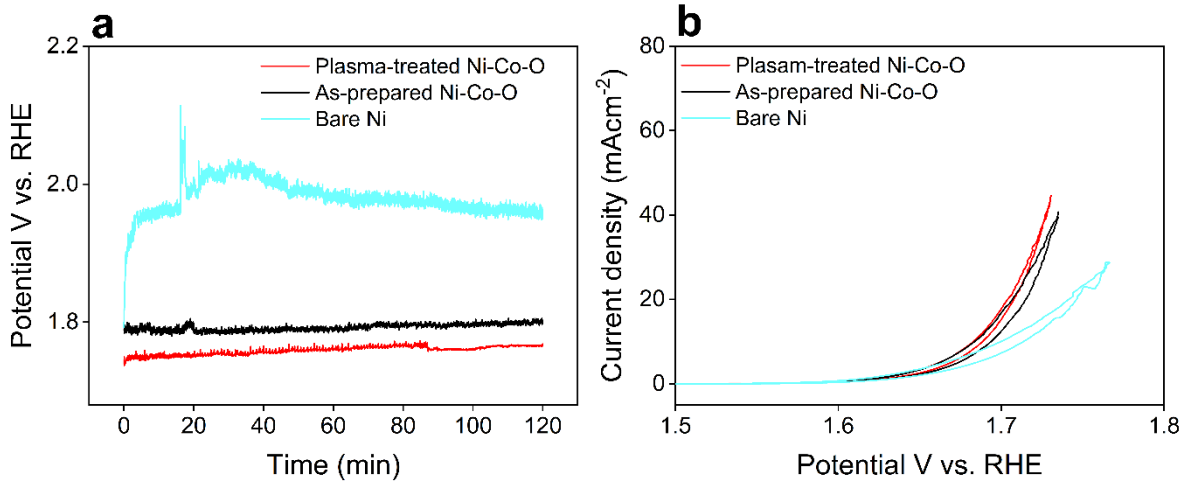

Figure S8 Electrochemical measurements in flow cell in 1 M KOH containing 15 ppb KOH (a) chronopotentiometry (CP) for 2 h at 100 mA cm^{-2} of as-prepared and plasma-treated Ni-Co-O electrodes (b) Cyclic Voltammetry (CV) activity curves recorded at the end of the protocol.

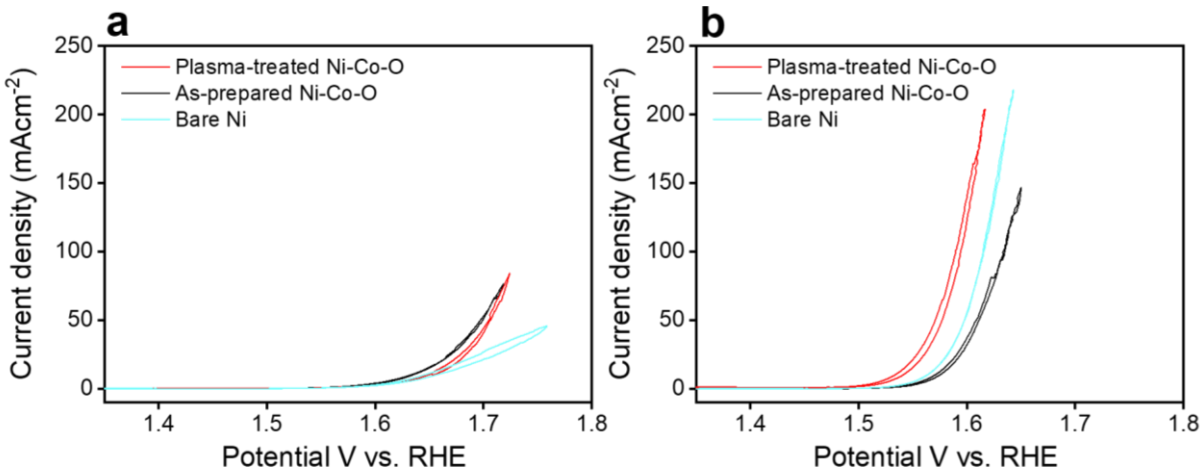

Figure S9 CV activity curves recorded at the end of the protocol (5 mVs-1, 1 V – 1.8 V vs. RHE), for as-prepared and plasma-treated Ni-Co-O electrodes, measured in a beaker cell with 1 M KOH containing either 15 ppb (a) or 110 ppb (b) Fe. The data represents the final of three cycles from a randomly selected sample within the respective triplicate measurements.

Table ST2 Double layer capacitance of the oxidative sweep for fast CV cycling obtained at a potential of 1.05 V vs. RHE. The potential was cycled five times between 1.-1.1 V vs. RHE with scan rates of 5 mV s-1, 10 mV s-1, 25 mV s-1, 50 mV s-1, and 100 mV s-1, respectively.

Sample	Double layer capacitance [mF]
Plasma-treated Ni-Co-O	2.25 ± 0.9
As prepared Ni-Co-O	0.13 ± 0.01
Bare Ni	0.13 ± 0.01

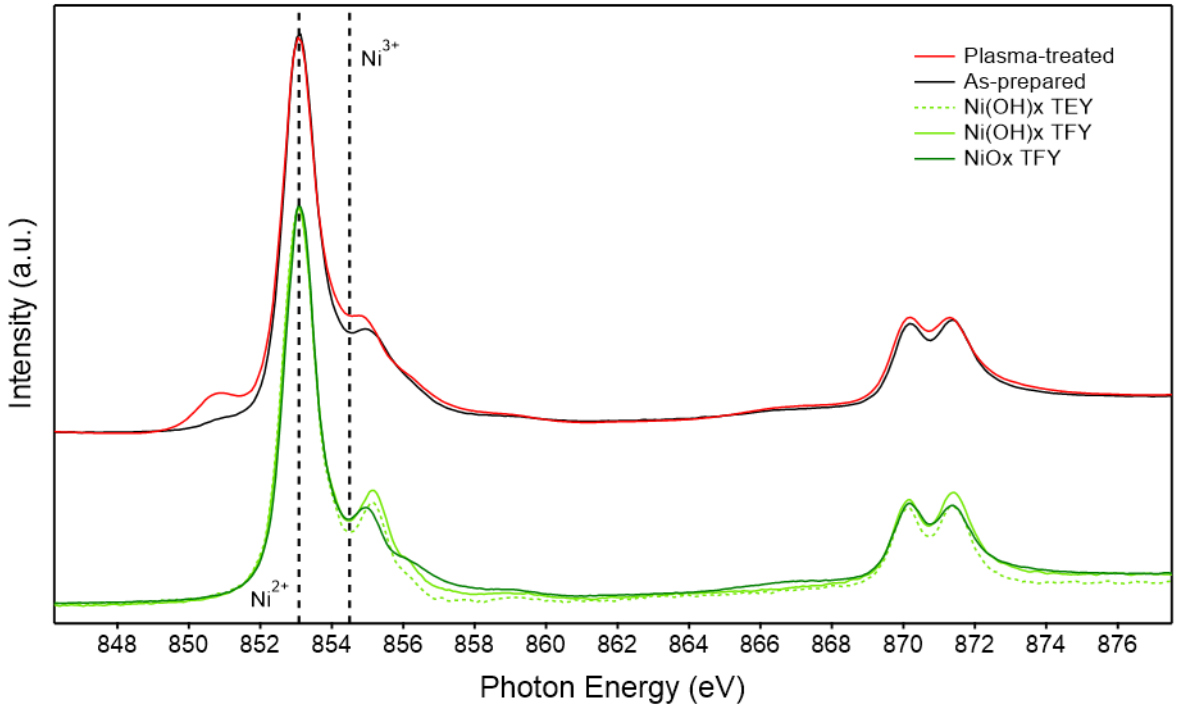

Figure S10 Averaged Ni L-edge spectra normalized to the maximum in comparison with reference spectra. The maxima of the measured spectra are shifted to match the main maxima of the reference spectra. The position of the maxima of the Ni^{2+} and Ni^{3+} L_3-edges are indicated by the wide-dashed lines.

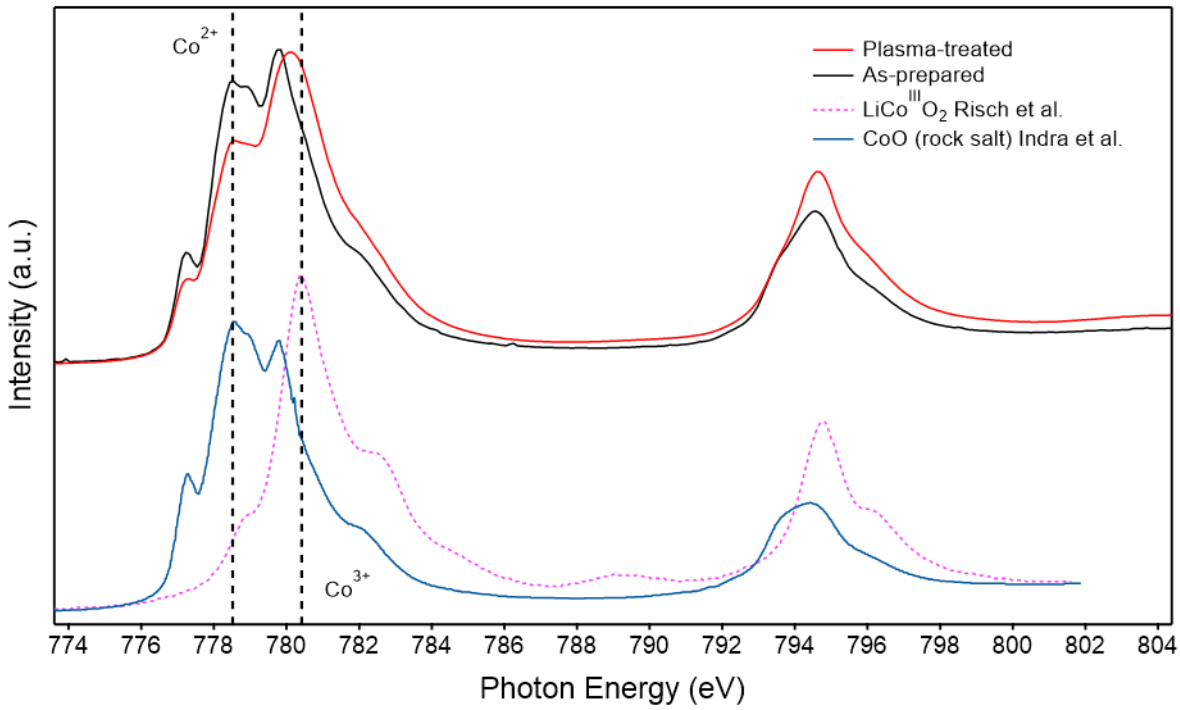

Figure S11 Averaged Co L-edge spectra normalized to the maximum in comparison with the reference spectra. The maxima of the measured spectra are shifted to match the main maxima of the reference spectra. Literature spectra are taken from Risch et al.[1] and Indra et al.[2] The position of the maxima of the Co2+ and Co3+ L3-edges are indicated by the wide-dashed lines.

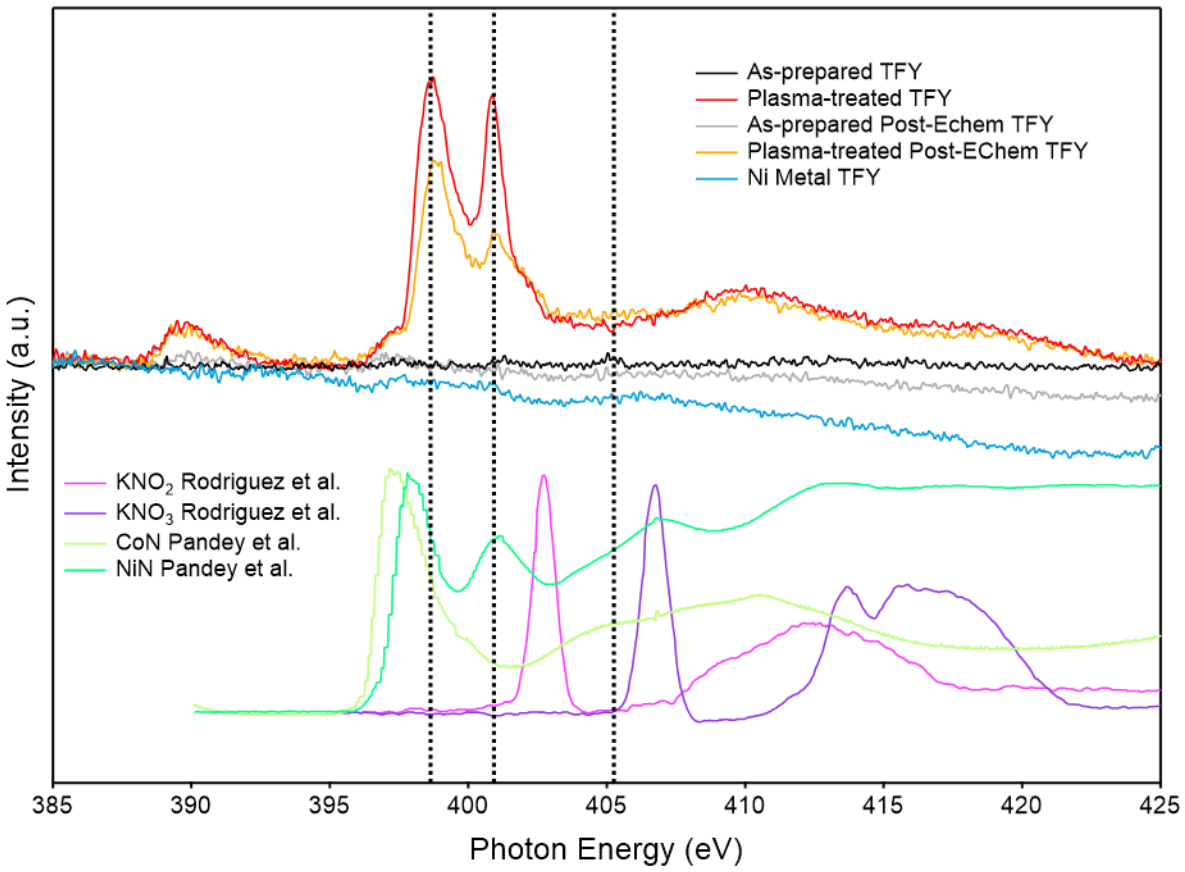

Figure S12 TFY spectra recorded across the nitrogen K-edge. Two individual spectra were recorded on each spot, two different spots were measured on each sample. This graph shows the averaged spectra of these four individual measurements for all four samples. No further correction was undertaken. The literature spectra are taken from Rodriguez et al.[3] and Pandey et al.[4]

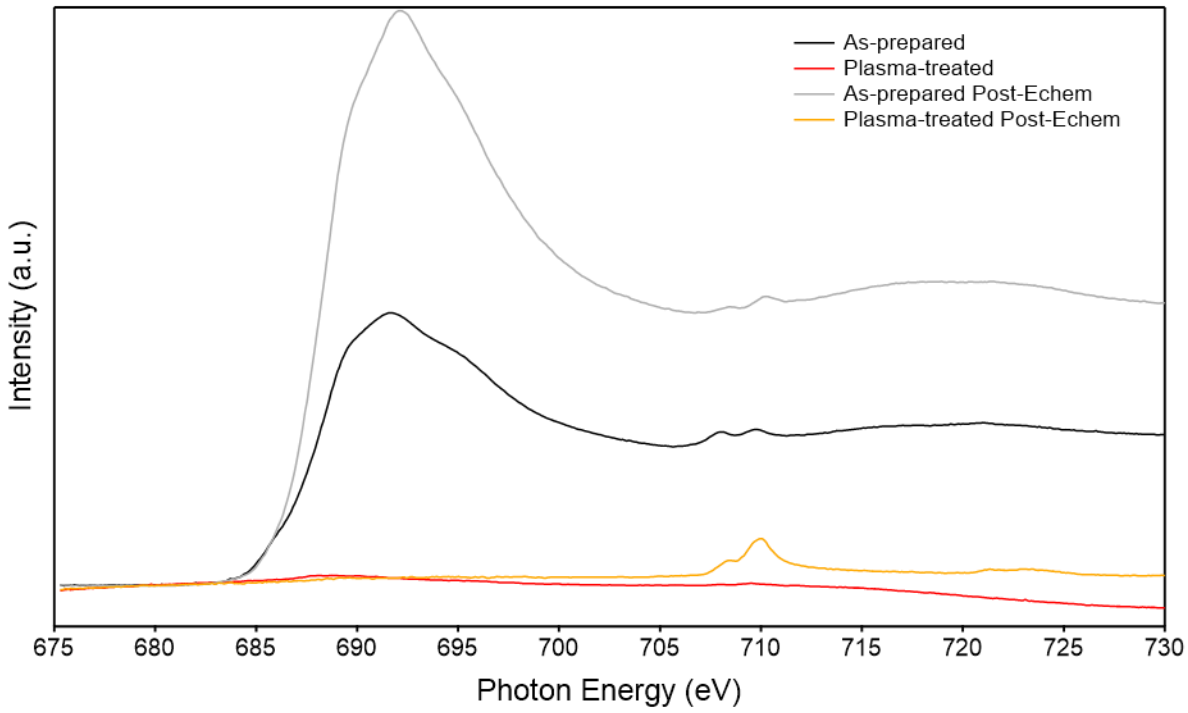

Figure S13 Two individual F K-edge TEY spectra were recorded on each spot, two different spots were measured on each sample. This graph shows the averaged spectra of these four individual measurements for all four samples. A linear background was subtracted. The energy calibration was stable between the measurements on one sample, but the energy shifts between different samples. This is probably no sample effect, but a feature of the ISISS beamline. The features at 710 eV are related to the Fe L_3-edge (see also Figure S18)

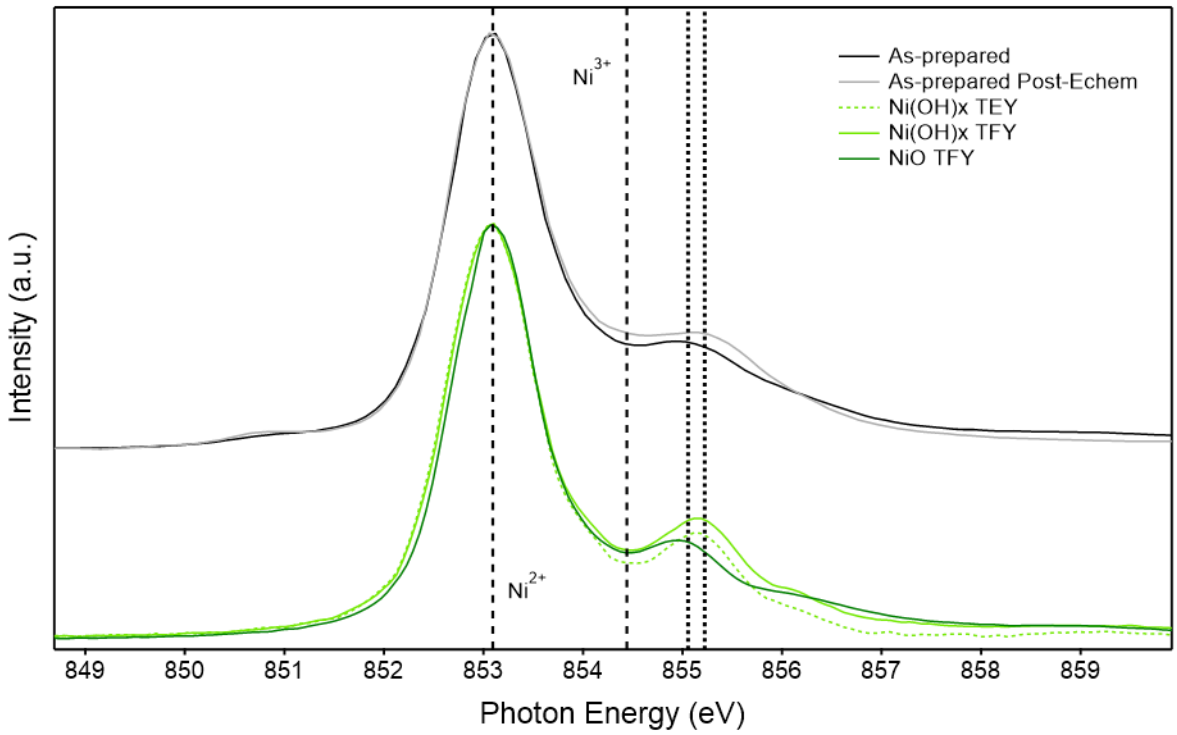

Figure S14 Averaged Ni L3-edge spectra normalized to the maximum in comparison with reference spectra. The maxima of the measured spectra are shifted to match the main maxima of the spectra measured on reference materials. The position of the maxima of the Ni^{2+} and Ni^{3+} L_3-edges are indicated by the wide-dashed lines.

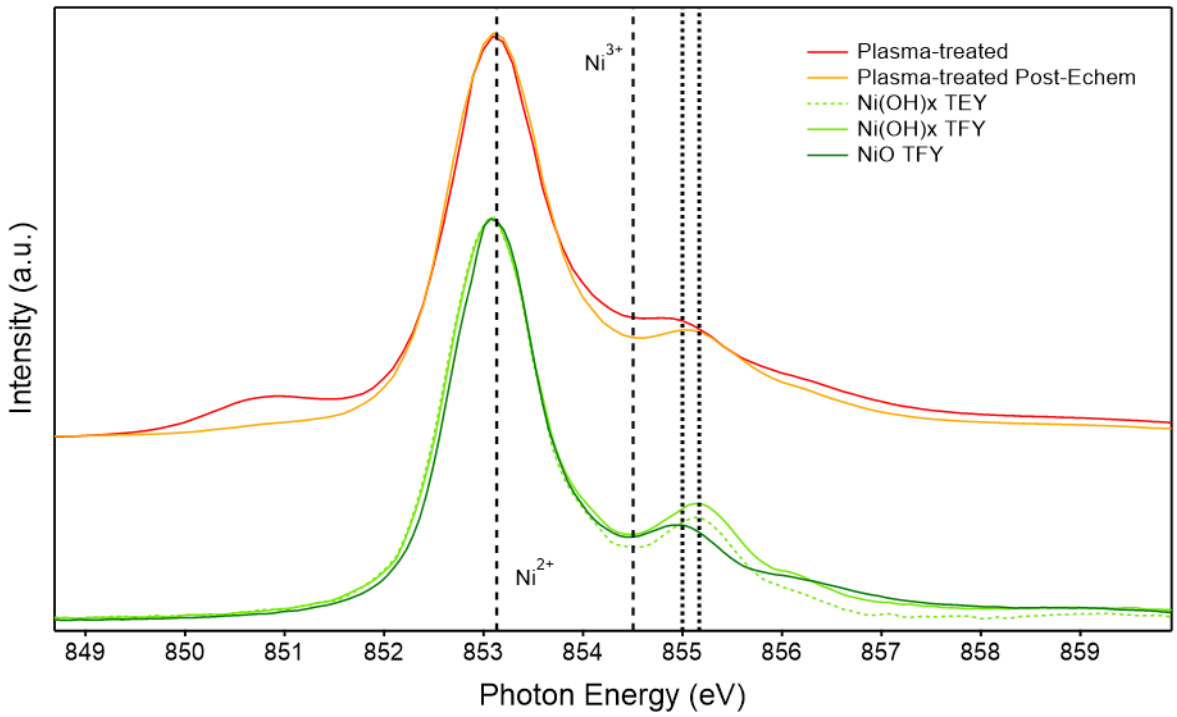

Figure S15 Figure S12 Averaged Ni L3-edge spectra normalized to the maximum in comparison with the reference spectra. The maxima of the measured spectra are shifted to match the main maxima of the reference spectra. The position of the maxima of the Ni^{2+} and Ni^{3+} L_3-edges are indicated by the wide-dashed lines.

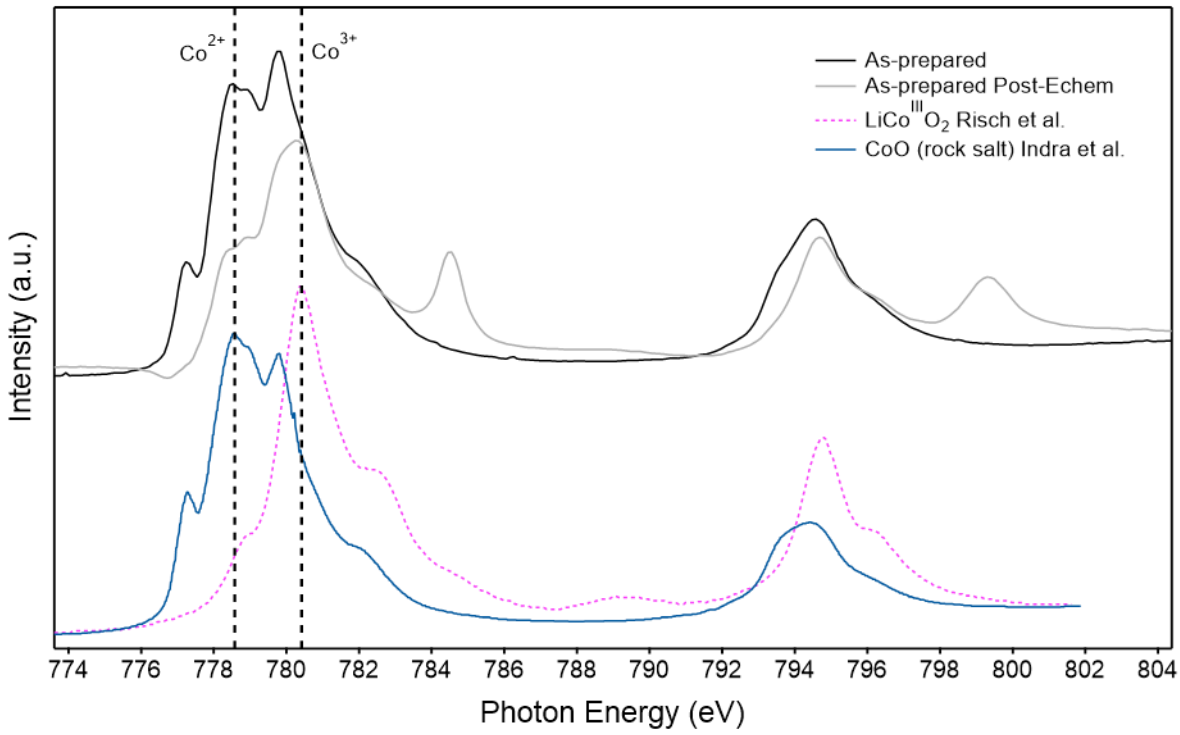

Figure S16 Averaged Co L-edge spectra (not scaled) in comparison with the reference spectra. The maxima of the measured spectra are shifted to match the main maximum of the reference spectra. Literature spectra taken from Risch et al.[1] and Indra et al.[2] The position of the maxima of the Co^{2+} and Co^{3+} L_3-edges are indicated by the wide-dashed lines.

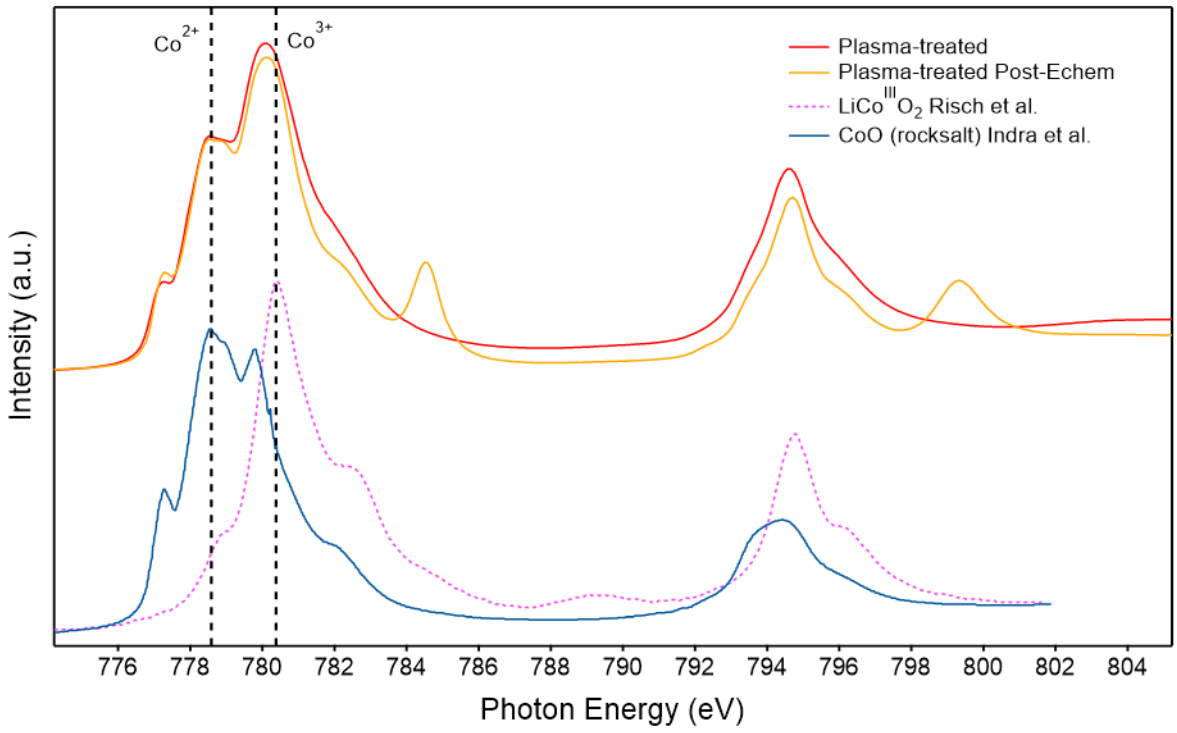

Figure S17 Averaged and scaled Co L-edge spectra in comparison with the reference spectra. The maxima of the measured spectra are shifted to match the main maxima of the reference spectra. Literature spectra taken from Risch et al.[1] and Indra et al.[2] The position of the maxima of the Co2+ and Co3+ L3-edges are indicated by the wide-dashed lines.

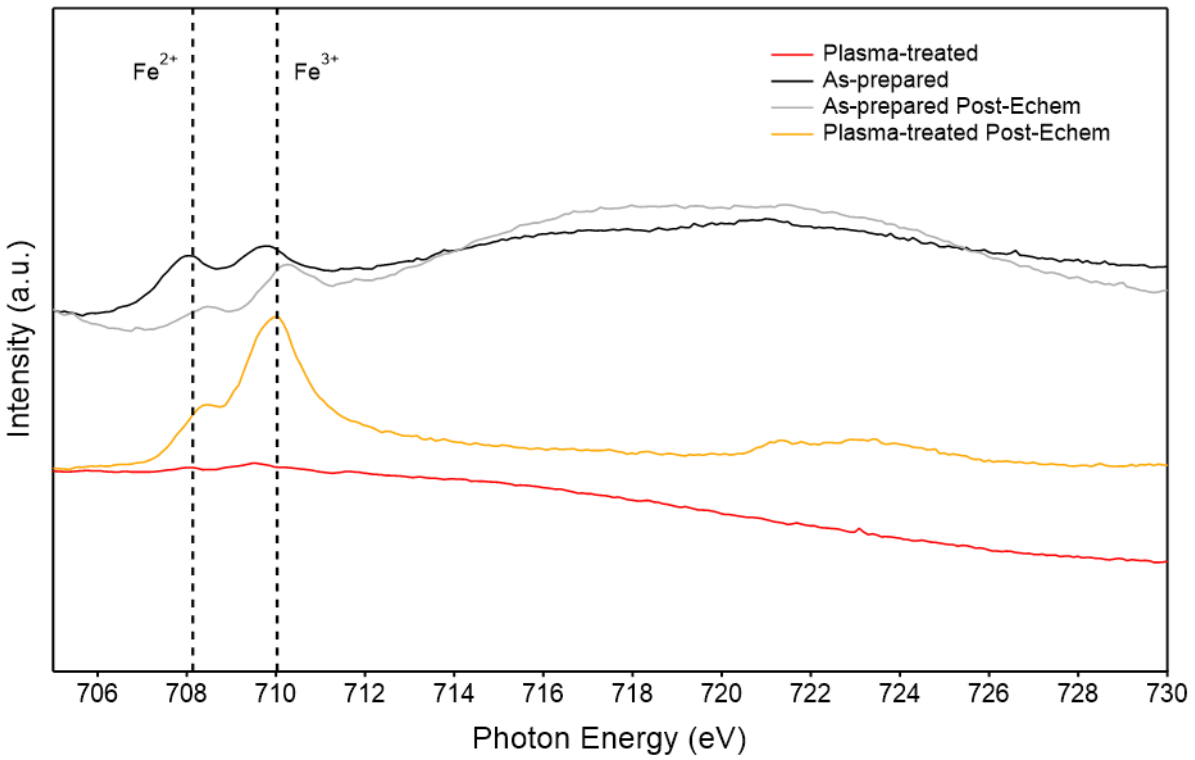

Figure S18 Averaged and scaled Fe L-edge spectra of the different samples. The position of the maxima of the Fe^{2+} and Fe^{3+} L_3-edges are indicated by the wide-dashed lines.

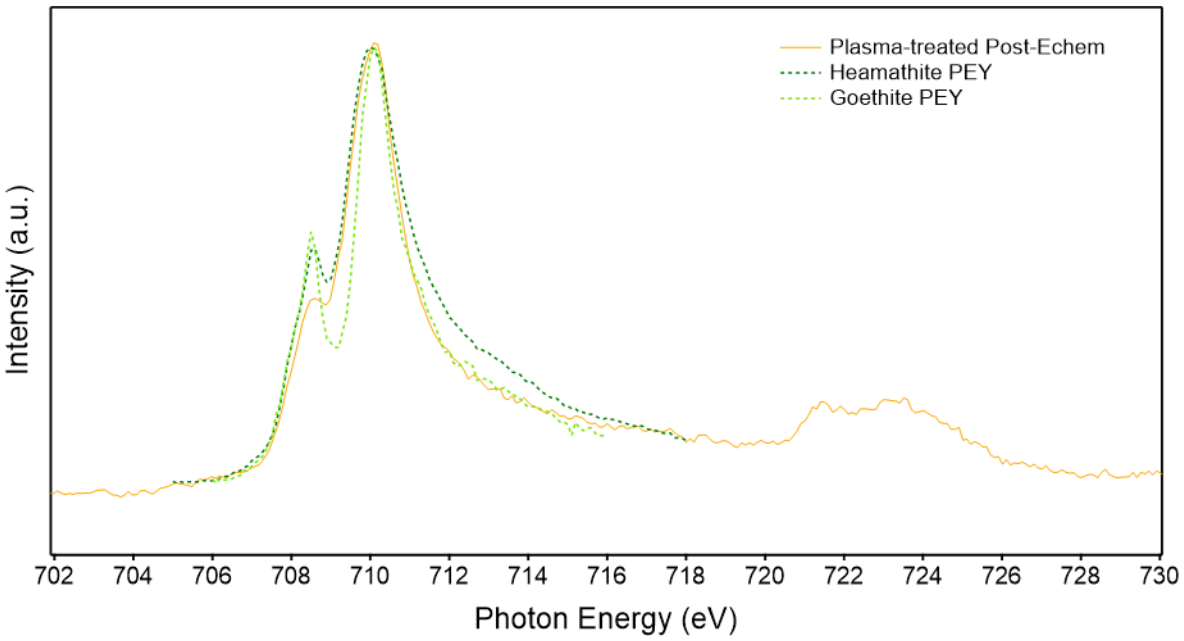

Figure S19 Averaged and scaled Fe L-edge spectrum of Plasma_Post Electrochemistry in comparison with reference spectra. The maxima of the measured spectra are shifted to match the main maxima of the reference spectra.

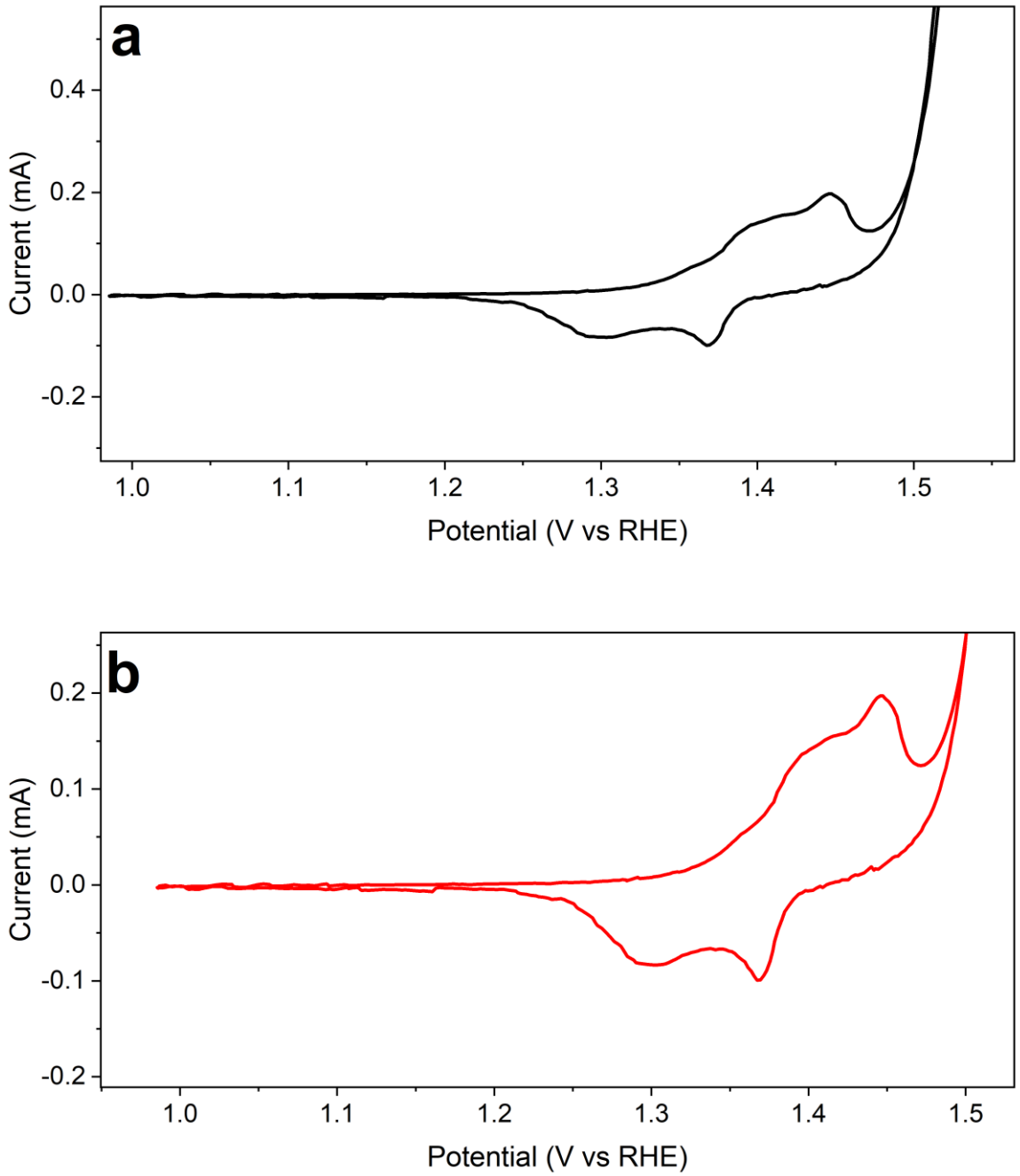

Figure S20 Cyclic voltammograms at a scan rate of 5 mv/s from the (a) as prepared and (b) plasma-treated Ni-Co-O films prior to the chronoamperometry measurements recorded during the operando Raman measurements.

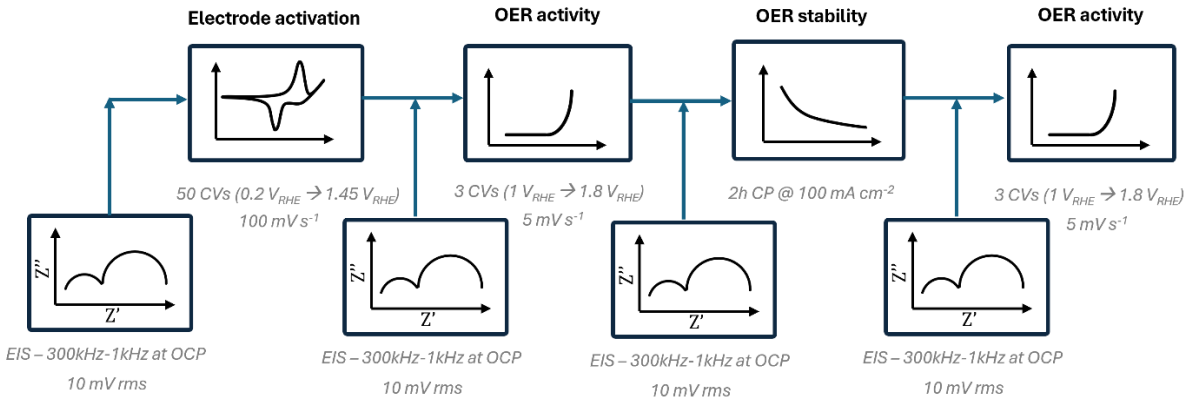

Figure S21 Scheme of the experimental protocol used for OER measurements with the beaker cell.

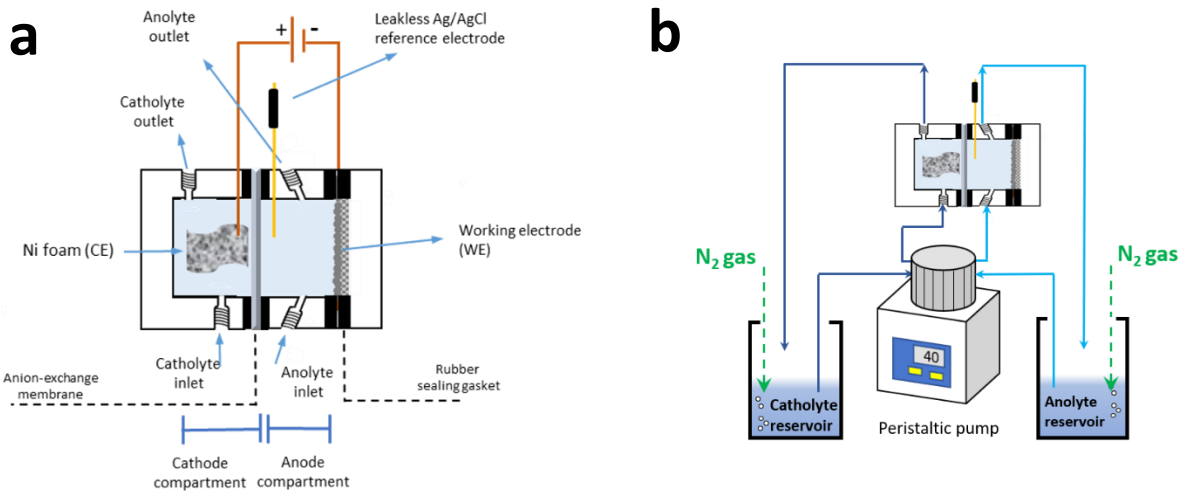

Figure S22 a) Scheme of the two-compartment batch electrochemical reactor (flow cell); b) Scheme of the experimental setup used for OER measurements with the flow cell.

References

(1) Risch, M.; Shevchenko, D.; Anderlund, M. F.; Styring, S.; Heidkamp, J.; Lange, K. M.; Thapper, A.; Zaharieva, I. Atomic Structure of Cobalt-Oxide Nanoparticles Active in Light-Driven Catalysis of Water Oxidation. Int. J. Hydrogen Energy 2012, 37 (10), 8878–8888. https://doi.org/10.1016/j.ijhydene.2012.01.138.

(2) Indra, A.; Menezes, P. W.; Das, C.; Göbel, C.; Tallarida, M.; Schmeiβer, D.; Driess, M. A Facile Corrosion Approach to the Synthesis of Highly Active CoOx Water Oxidation Catalysts. J. Mater. Chem. A 2017, 5 (10), 5171–5177. https://doi.org/10.1039/c6ta10650a.

(3) Rodriguez, J. A.; Jirsak, T.; Dvorak, J.; Sambasivan, S.; Fischer, D. Reaction of NO2 with Zn and ZnO: Photoemission, XANES, and Density Functional Studies on the Formation of NO3. J. Phys. Chem. B 2000, 104 (2), 319–328. https://doi.org/10.1021/jp993224g.

(4) Pandey, N.; Gupta, M.; Phase, D. M.; Gupta, A. In Situ N K-Edge XANES Study of Iron, Cobalt and Nickel Nitride Thin Films. J. Synchrotron Radiat. 2021, 28, 1504–1510. https://doi.org/10.1107/S1600577521006822.